Microstructure estimation and validation of ER110S-G steel structures produced by wire and arc additive manufacturing

Mishra, V.; Babu, A.; Schreurs, R.; Wu, K.; Hermans, M. J.M.; Ayas, C.

Important note
To cite this publication, please use the final published version (if applicable).
Please check the document version above.

Original Article

Microstructure estimation and validation of *ER110S-G* steel structures produced by wire and arc additive manufacturing

V. Mishra [*,1], A. Babu [**,1], R. Schreurs, K. Wu, M.J.M. Hermans, C. Ayas [***]

Mechanical, Maritime and Materials Engineering, Delft University of Technology, Mekelweg 2, 2628 CD, Delft, the Netherlands

ABSTRACT

Wire and Arc Additive Manufacturing (WAAM) emerged as a manufacturing process for large scale structures with extensive form and design freedom. WAAM can be fully exploited once the relation between the transient thermal history and its relation to microstructure development and resultant mechanical properties is established. This relation can be further used for computational design tools such as Topology Optimization. This paper presents a model to predict the relation between the thermal history and solid-state phase transformations in a widely applicable High Strength Low Alloy steel ER110S-G. The transient thermal history of parts manufactured by WAAM is modelled using finite element analysis. The modelled thermal history is validated with thermocouple measurements. Our results show that a critical cooling cycle is responsible for the solid-state phase transformation in an AM part. The cooling rate of this particular cooling cycle is superimposed onto an experimentally constructed Continuous Cooling Transformation (CCT) diagram to determine the local solid-state phase fractions. The predicted phase fractions in three wall samples with different design and processing conditions of AM parts are used to predict the hardness. The predicted hardness is 10% higher than the measured hardness of AM samples. The effect of tempering is also considered in the model through JMAK equation. The results show that the tempering is caused in regions with high martensite content and it lowers the hardness by 8 − 10%. The micrographs of the AM parts show that the microstructural features are same for the AM parts with similar critical cooling rates.

© 2023 The Author(s). Published by Elsevier B.V. This is an open access article under the CC BY license (http://creativecommons.org/licenses/by/4.0/).

1.   Introduction

Wire and Arc Additive Manufacturing (WAAM) has recently emerged as a novel manufacturing method with extensive form freedom for large-scale structures, especially in maritime and aerospace applications [1,2]. In WAAM, the metal wire is melted by an electric arc and deposited along predefined paths. The deposition typically happens layer-by-layer starting on a substrate, as schematically shown in Fig. 1. WAAM has been employed for a wide range of metallic materials including Titanium alloys, Nickel based alloys, Aluminum alloys, and Steels [3]. WAAM technology is currently used to manufacture shapes that are not feasible for conventional manufacturing technologies with milling and casting.

Topology Optimization (TO) is a computational design tool through which optimal geometric layout of a component with enhanced mechanical performance is determined [4], and TO designs are typically geometrically complex. Near net shape of complex structures can be realised by WAAM with high dimensional accuracy [5—9]. TO in conjunction with WAAM can be used to utilise the potential of manufacturing technology [10].

The mechanical properties of these metal WAAM parts can vary significantly depending on the microstructural development during the manufacturing process, as a result of the complex thermal history [11—14]. The material locally experiences multiple thermal cycles depending on the design features, deposition strategies, process conditions, and material properties. The most common design studied is a simple wall. The thermal history experienced by such a simple wall is numerically evaluated and experimentally measured [15—18]. Even for a simple thin wall, as shown in Fig. 1, the thermal history experienced by material points is substantially different at different wall locations. For example, near the substrate, multiple heating, and cooling cycles are experienced, whereas the topmost layer of the wall experiences only a single heating and cooling cycle. The material deposited near the substrate exhibits a higher hardness than the

material deposited farther away. This is because the substrate acts as a heat sink and facilitates rapid cooling for the material points close to it, leading to a microstructure with a dominant martensite phase [15]. However, the effect of the substrate for material points further away from it diminishes, causing a reduction in cooling rates and a reduction in the martensite phase fraction [19—21]. Thin walls intersecting at a junction are also studied [22,23]. These studies conclude that since there is more material in the proximity of the junction local thermal diffusivity is high, which facilitates heat towards the base plate at the junction compared to regions far away. The design-induced thermal inhomogeneity is also partially due to the number of times the junction is in contact with the heat source compared to the material points far away from the junction. Heat accumulation due to local design change also leads to low cooling rates [24].

Apart from the local design features, process parameters that influence the thermal history are wire feed rate, travel speed of the heat source, inter-pass dwell time, and the associated inter-pass temperature. The heat input is proportional to the ratio of wire feed rate and travel speed [11,15,25]. Consequently, variation in the heat input can lead to variations in the microstructure [15]. Inter-pass dwell time is the duration between the end and initiation of two subsequent layers. Increasing the inter-pass dwell time allows more time for the part to cool down. For thin walls, increasing the dwell time can result in a more uniform microstructure because the thermal conditions of the deposited material and pre-deposited material would remain the same for every layer [26]. However, increasing dwell time increases the duration of manufacturing and therefore implies a higher cost of production [27]. Inter-pass temperature is the temperature at which the deposition of the next layer starts. It is observed that a thin wall structure manufactured with high inter-pass temperature, leads to a thermal condition where the material experiences high temperatures for a longer time. For steels, the cooling rates reported at the high inter-pass temperature are low. The low cooling rate results in solid-state phases with lower strength which reduces the overall yield strength of the manufactured part [28]. The deposition pattern
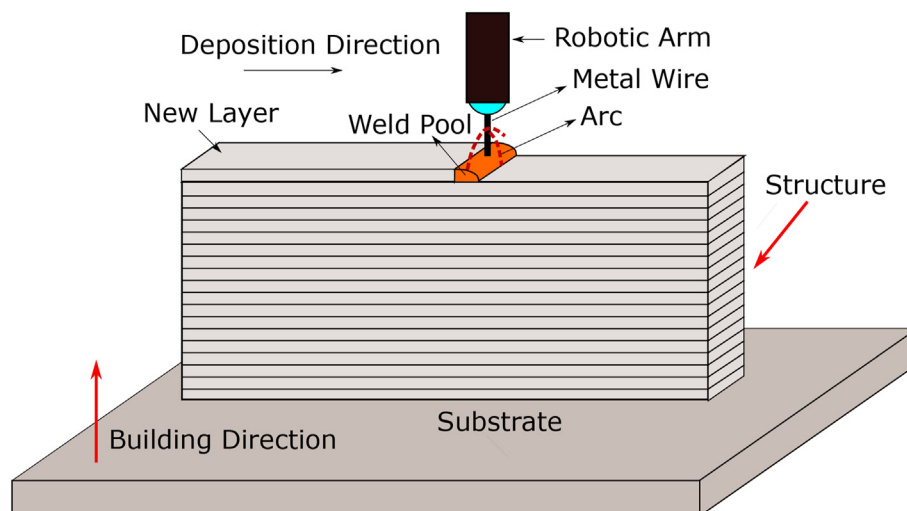

Fig. 1 — Schematic representation of the WAAM process of a thin wall in a layer-by-layer manner.
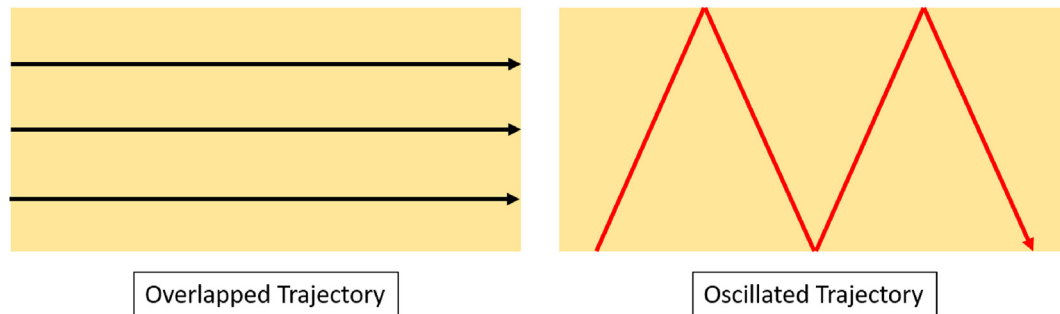
Fig. 2 – **Schematic illustration of deposition paths of the overlapping and oscillating deposition strategies used by** *Aldalur* **et al. [14] to investigate their effect on the mechanical properties.**

also influences the thermal history experienced throughout the part. Thin wall structures produced by deposition patterns with overlapping and oscillating strategies, shown in Fig. 2, show that the oscillating strategy leads to lower cooling rates than the overlapping strategy [14,29]. This is because, with an oscillating strategy, the frequency of the heat source returning to the same material point is higher than that of the overlapping strategy, consequently leading to higher temperatures and lower cooling rates, hardness, and strength. This could be attributed to the presence of a high fraction of the soft ferrite phase.

Our aim is to establish the relationship between the thermal history obtained from the WAAM process and the resulting mechanical properties. This will pave the way to use this particular relation in to generate designs with desired properties. A requirement for TO is that a simulation correlating between a physical quantity and resulting properties should be computationally inexpensive. This is because of the iterative nature of the optimization process typically consisting of hundreds of iterations and the simulation performed for each iteration of the optimization.

We choose to study the effect of the WAAM process on High-Strength Low Alloy (HSLA) steel ER110S-G, which exhibits excellent weldability and is suitable for the WAAM process [30]. Microstructure of HSLA steel encompasses various aspects such as grain size and morphology, crystallographic texture, solid-state phases, and tempering effects, all dictated by the transient thermal history. The combination of thermal gradients in the melt pool and solidification rates determines the grain size and morphologies [31]. After solidification, the formation of predominantly columnar grains of the austenite phase (γ) commences in HSLA steels. Once the austenite is formed, solid-state phase transformations of interest begin. Below the critical temperature Ac_3, the austenite (γ) transforms to a phase mixture containing various morphologies of ferrite (α) (polygonal ferrite, upper bainite, and acicular ferrite) and martensite (α_m). These solid-state phases significantly control mechanical properties such as strength and ductility [32,33]. The formation of each of these phases depends on the cooling rate austenite encounters. Martensite can further transform into tempered martensite, given it is held above a critical tempering temperature. It has been reported that there is no preferred orientation or strong texture in the WAAM printed HSLA steels resulting in isotropic mechanical properties [15,34–36].

Various modelling approaches can be used to model various aspects of microstructure. To understand microstructure development in detail cellular automata models [37–39], phase field model [40], kinetic monte carlo model [41] and representative volume method [42] can be used. These models provide a detailed representation of the microstructure development but are computationally expensive, which makes them unsuitable for optimization study. Therefore, we choose a finite element-based model to evaluate the transient thermal history and correlate it to the material properties. Since there are no strict models that can predict the phase transformation and tempering kinetics for HSLA steels, therefore, our objective in this particular study is to model the solid-state phase transformation and the effect of tempering of a WAAM-manufactured HSLA part and validate it through experiments. Thus, we set aside the considerations related to grain size, and morphology for simplicity. Hereon, the terminology microstructure refers to solid-state phases and its their phase fractions. For the powder bed AM process, Zhang et al. [43] estimated the metallurgical phases of Steel 5140. However, no experimental validation is reported. Also, the effect of tempering is not accounted for in their analysis.

In this study, the deposition process in WAAM is simulated using the finite element activation method, and the heat added to the material is modelled using the Double Ellipsoid Goldak heat source [44]. A finite element analysis is performed to determine the thermal history. The thermal history obtained from the simulation is validated by the temperature measured through multiple thermocouples during the actual printing of these parts. The critical cooling rate responsible for the solid-state phase transformation from the thermal history is identified. A Continuous Cooling Transformation (CCT) diagram is constructed from dilatometry experiments and used for estimating the phase fractions of the metallurgical phases due to the corresponding simulated critical cooling rate of the material points for the entire part. After that, the tempering of the martensite phase is accounted for through the Johnson-Mehl-Avrami-Kohnogorov (JMAK) equation. A series of tempering experiments are done in which the samples are placed at isothermal temperatures for a fixed time to calibrate the JMAK equation. This equation is then applied to the transient thermal history obtained from WAAM simulations. Finally, the estimated phase fractions of the metallurgical phases are used to predict the microhardness of the part using empirical relations from the literature [45]. These estimated

values are compared to the experimentally measured hardness values.

Details on the experimental setup and part geometries studied in this paper are outlined in Section 2. Description of the thermal modelling is given in Section 3. The procedure for predicting the fraction and morphology of the solid-state phases is explained in Section 4. The results obtained are given in Section 5. Finally, the most salient points of the study are reiterated in Section 6.

2. Experimental setup

2.1. Part geometries and deposition strategy

The schematic representations of the geometric layouts of the parts are shown in Fig. 3. Three walls are manufactured. Simple walls shown in Fig. 3a are produced with two different welding conditions. The tapered wall is produced with a single set of welding conditions to study the effect of design on the microstructure. As deposition progresses, the geometric layout of the tapered wall facilitates faster cooling compared to the simple wall. Therefore, the effect of tapering on the microstructure is also investigated. The full description of the process parameters is given in Table 1. The deposition strategy for printing is based on bidirectional deposition, i.e. the deposition direction is reversed after completion of a layer as indicated in Fig. 3. For each geometry, 20 single bead layers are deposited. The bead height (h) and bead thickness (t) corresponding to each geometry are

also given in Table 1. During the experiments, four thermocouples are attached to each wall, and the locations of the thermocouples are indicated with black dots in Fig. 3. From here on, the three samples are referred to as thick, thin, and tapered walls as given in Table 1. Preliminary single bead experiments are performed, and a process parameter window is identified [46]. Two sets of process parameters are selected from this process parameter window. Deposition of thick and thin wall structures is achieved with a constant travel speed of 8 mm/s and wire-feed rate of 4.5 m/min and 2 m/min, respectively. The tapered wall comprises bidirectionally deposited 20 layers with a 120 mm long initial layer. A 45° tapering is achieved in the tapered wall by offsetting the beads' start and stopping by 1.6 mm in subsequent layers. Each bead for all the walls is deposited with an approximate inter-layer time of 120 s. The inter-layer time of approximately 600 s is taken after the layers in which thermocouples are attached.

2.2. Setup and material

Thick, thin and tapered walls are fabricated by a Fanuc 5-axis robot system integrated with a Fronius 5000CMT-i power source. The first layer of the walls is deposited on an ER110S-G steel substrate of 250 mm × 80 mm × 25 mm. The composition of the high strength steel wire (LNMoNiVa) with a diameter of 1.2 mm from Lincoln Electric used for the WAAM experiments is provided in Table 2. The density ρ, the heat capacity c_p, and the conductivity κ of the steel as a function of temperature are given in Fig. 4 [47]. The peak of specific heat of the material at
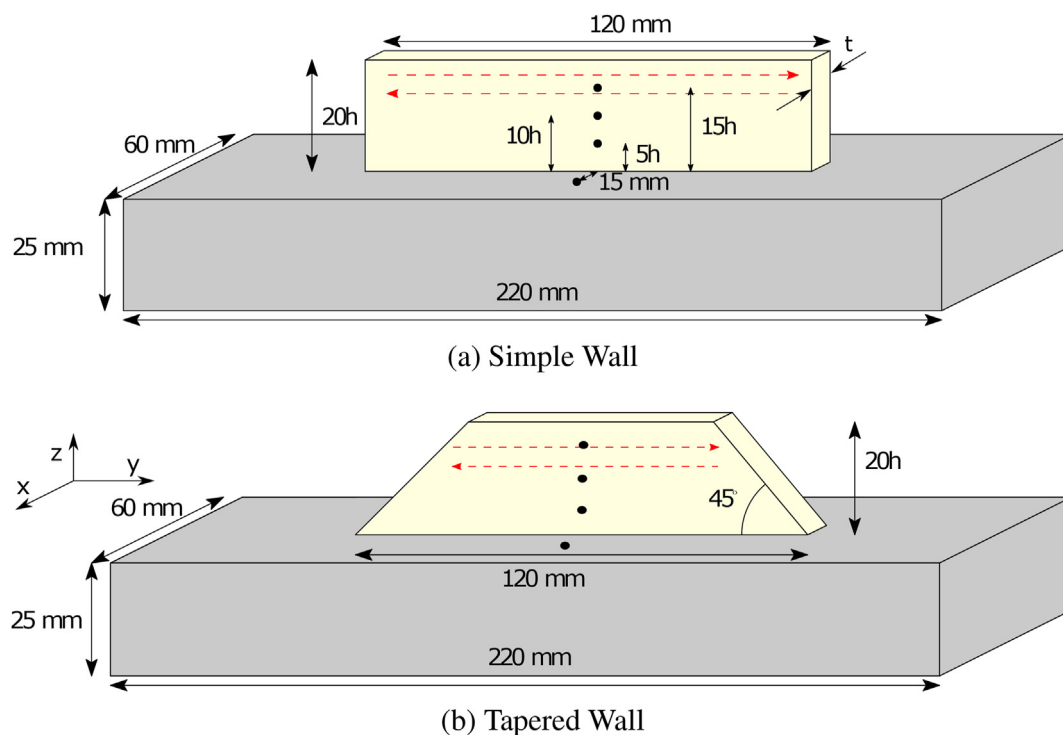

(a) Simple Wall

(b) Tapered Wall

Fig. 3 — **Schematic illustration of the layout of the parts investigated. The deposition strategy is shown with red arrows. The thermocouples indicated with black dots are attached to the substrate at the 5th layer, 10th layer, and 15th layer.**

Table 1 − Process parameters used for manufacturing the parts.

Specimen	Geometry	WFR (m/min)	TS (mm/s)	h (mm)	t (mm)	# of layers
S1	Thick Wall	4.5	8.0	1.43	8.35	20
S2	Thin Wall	2.0	8.0	1.23	4.73	20
S3	Tapered Wall	4.5	8.0	1.43	8.35	20

the transformation temperature is used to model heat dissipation and generation during phase transformation. Pulsed mode deposition is used as the metal transfer mode. A mixture of 82% argon and 18% carbon dioxide is used as the shielding gas with a flow rate of 17 l/min. During welding a contact tip-to-work piece distance (CTWD) of 15 mm is maintained.

2.3. Process monitoring

Current and voltage characteristics are measured at 5 kHz frequency during the deposition using a Triton 4000 data acquisition system. Linear heat input (HI) corresponding to the process parameters used is determined from the measured current and voltage data according to

$$HI = \frac{\eta \Sigma_{i=0}^{n} V_i I_i n}{TS}, \tag{1}$$

where V_i is the instantaneous voltage measured at i^{th} time instance, I_i is the instantaneous current, n is the total number of measurements, TS is the travel speed, and η is the arc efficiency. The arc efficiency depends upon the processing conditions and is generally in the range of $0.75 − 0.90$ [48]. K-type thermocouples are attached to the substrate and the part during the WAAM process (see also Fig. 3a). Time−temperature data from the thermocouples are recorded with a DL75 scope at a sampling rate of 500 Hz. The height of all the 20 layer samples is measured at three locations and then averaged to estimate the layer height. This layer height is further used in the thermal model to simulate the deposition of the individual layers.

2.4. Dilatometry experiments

Continuous cooling and tempering experiments are performed in a Bahr 805 DIL A/D dilatometer. Samples of 10 mm × 4 mm × 2 mm are extracted from a WAAM deposited ER110S-G block by wire electron discharge machining. A K-type thermocouple is attached to the centre of the block, which acts as the control thermocouple for executing the controlled thermal profiles.

Table 2 − Composition of high-strength steel wire (LNMoNiVa) as provided by the supplier.

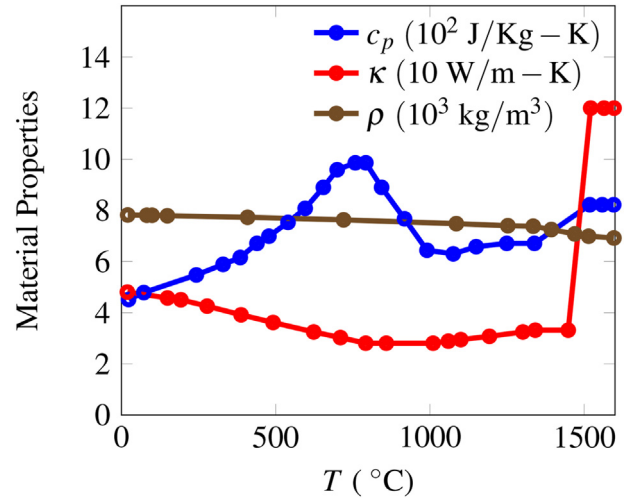| Element	C	Mn	Ni	Si	Cr	Mo	Cu	V	Fe
Weight percentage	0.09	1.7	1.4	0.54	0.3	0.24	0.06	0.08	Balance

Fig. 4 − Thermal material properties of HSLA ER110S-G steel used for thermal simulations [47].

2.4.1. Continuous cooling experiments

Continuous cooling transformation diagrams (CCT) are generally constructed experimentally by sequentially heating the steel grade of interest to austenitisation temperatures and then subjecting it to controlled cooling rates. Samples are heated to 900 °C at 20 °C/s and held at 900 °C for 120 s for full austenitisation. The samples are subsequently cooled down to room temperature at 5, 10, 20, 30, 40, 50, 75 and 330 °C/s. The dilatometer recorded the change in length of the samples as a result of thermal expansion and phase transformation with temperature. The temperature versus dilation plot is illustrated in Fig. 5. During cooling from 900 °C, regions devoid of phase transformations are indicated by linear dilation. Phase transformation temperatures are determined by identifying the temperature at which the temperature versus dilation plot deviates from its linear behaviour. The lever rule is applied to the dilatometry data to assess the phase fraction of the austenite remaining at a particular temperature. The application of the lever rule is based on two assumptions.
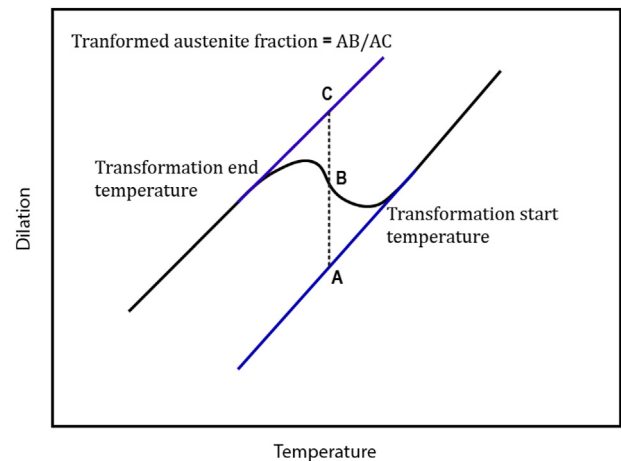

Fig. 5 − Illustration of dilatometry data during austenite decomposition.

- Partitioning of elements during cooling is ignored.
- Volume change associated with the measured dilation is isotropic [49].

As indicated in Fig. 5, the relative position of the dilatometric curve between the extrapolated linear regions of austenite and ferrite enables estimation of the transformed austenite fraction with temperature [50].

Moreover, we assume that the alloying is homogeneous in our dilatometry sample. The validity of this assumption is confirmed by the Energy Dispersive Spectroscopy (EDS) of the dilatometry samples. The result showed no significant variation in the alloying elements compared to the specified percentage of the alloys in Table 2.

2.4.2. Tempering experiments

Tempering experiments on WAAM printed ER110S-G HSLA are performed to develop a phenomenological model to predict tempering kinetics. Since tempering is associated with martensite, the sample is heated to the austenitic temperature of 900 °C, held for 120 s, and quenched to room temperature. A high cooling rate during quenching ensures that a fully martensitic microstructure is obtained. The sample is subsequently heated to temperatures such as 700 °C, 550 °C and 400 °C, which lie in the tempering zone. The samples are held at the tempering temperature for 5 s, 120 s and 1800 s and then quenched to room temperature. Due to tempering, the hardness of the samples reduce. The reduction in hardness due to tempering is a function of the tempering temperature and duration and can be modelled using the JMAK equation. To model the tempering kinetics using the JMAK equation, it is imperative to know the hardness of the fully tempered martensite. For this purpose, one dilatometry sample is austenised, quenched to room temperature, and then subjected to a tempering treatment at 700 °C for 5 h.

2.5. Microstructural characterisation

Transverse cross-sections are extracted from the centre of thick, thin, and tapered walls for micro-hardness measurements. Samples are prepared by grinding and polishing with colloidal silica paste of 1 μm and 3 μm particle size. A 2% Nital solution is utilised for etching, and microstructural features are observed via optical microscopy. Vickers micro-hardness measurements are made along the build direction of the deposited samples with a load of 1 kg. In the case of the dilatometry samples from the continuous cooling and tempering experiments, hardness measurements with a load of 1 kg are made at 10 points on each sample and averaged.

3. Thermal modelling

During the WAAM process, the heat transfer from the newly deposited hot metal to the rest of the part and substrate occurs by conduction. In contrast, heat transfer to the surroundings occurs through convection and radiation. In Section 3.1, heat transfer equations solved numerically to simulate the heat transfer during the deposition process are given. As mentioned previously, the WAAM process consists of two aspects, local heating of the part with a moving heat source and material deposition. Heat addition is modelled through the Goldak heat source model [44]. The Goldak heat source model is briefly described in Section 3.2. The material addition is simulated by the finite element activation method described in Section 3.3.

3.1. Heat transfer equation

The governing equation for heat transfer through conduction is given by

$$\frac{\partial(\rho c_p T)}{\partial t} = \nabla \cdot (\kappa \nabla T) + \dot{Q}. \tag{2}$$

Here, T and t are the temperature and time, while ρ, c_p and κ are the density, specific heat capacity and thermal conductivity of the material, respectively. $\dot{Q}$ is the power per unit volume added to the part, in this case representing the electric arc, which is modelled using the Goldak heat source model [44] explained in the next section.

The heat flux $\mathbf{j}$ from the part to the surroundings is governed by

$$\mathbf{n} \cdot \mathbf{j} = h_c(T - T_a) + \epsilon\sigma(T^4 - T_a^4). \tag{3}$$

Here, $\mathbf{n}$ is the unit outward normal of the surface from which heat transfer occurs. h_c is the convective heat transfer coefficient, ϵ is the material emissivity, and σ is the Stefan—Boltzmann constant (5.6703×10^{-8} W/m^{2}K^4). T_a is the ambient temperature of the surrounding.

3.2. Double ellipsoidal goldak heat source model

The Double Ellipsoidal Goldak heat source model [44] is widely used in welding and WAAM [51], to mimic the heat addition. In the Goldak heat source model, the complexity of the weld pool and the heat transfer phenomenon therein are simplified by a double ellipsoidal heat distribution schematically shown in Fig. 6.

The heat distribution inside a general ellipsoid is given as

$$\dot{Q}(x, y, z, t) = \frac{6\sqrt{3}\eta VIf}{abc\pi\sqrt{\pi}} \exp\left(-\frac{3(y - v_s t)^2}{a^2} \right.$$
$$\left. -\frac{3x^2}{b^2} - \frac{3z^2}{c^2}\right). \tag{4}$$

Here, $\dot{Q}$ is the power per unit volume given for a general ellipsoid where a, b and c are the half-length, half-width and half depth of an ellipsoid. V and I are the voltage and current, respectively. η is the efficiency of the heat source, which typically ranges from 0.8 to 0.9 [51]. In the Goldak heat source model, the front and rear of the weld pool are approximated by combinations of quarters of two general ellipsoids. The front and rear ellipsoid are of different shapes; therefore, the half-length of the ellipsoid is a_f and a_r representing the front and rear length of the weld pool, respectively. b and c are the same for both ellipsoids. $\dot{Q}_f$ and $\dot{Q}_r$ are the power per unit volume distributed over the front and rear ellipsoids as shown in Fig. 6. The dimensions of the front and rear arc are substituted in Eq. (4) to calculate the distribution of power per unit volume $\dot{Q}_f$ and $\dot{Q}_r$ over the front and rear end,
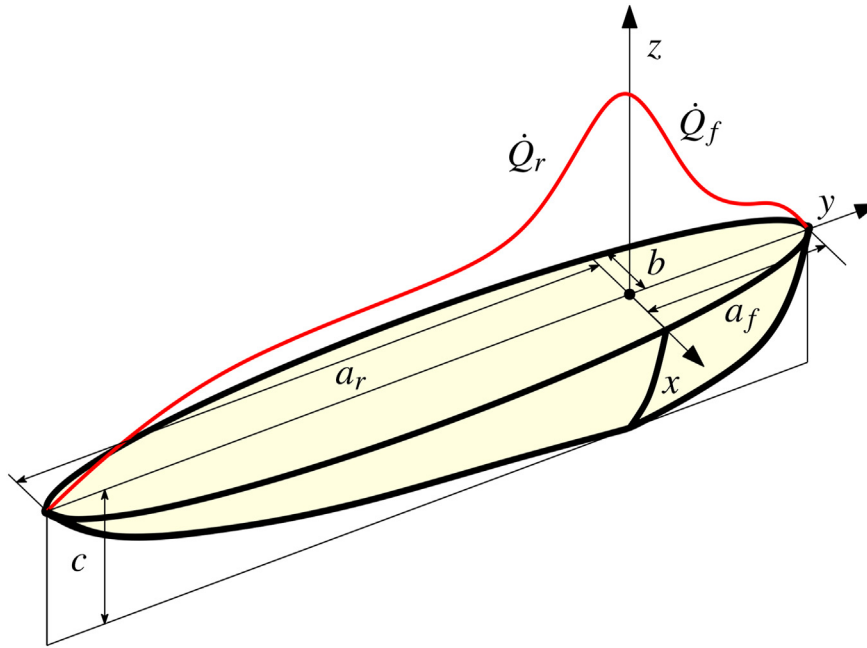
Fig. 6 — Schematic representation of the Goldak heat source [44] to model the heat addition process during WAAM. $\dot{Q}_r$ and $\dot{Q}_f$ is the power per unit volume given in Eq. (4) for the rear and front regions with respect to the origin, which is schematically represented by the red curve.

respectively. The factor f represents the fraction of power attributed to an ellipsoid. f_f and f_r are power factors associated with the front and rear ellipsoid. These factors are calculated as

$$f_f = \frac{2a_f}{a_f + a_r}, \qquad f_r = \frac{2a_r}{a_f + a_r}. \tag{5}$$

3.3. Finite element analysis and element activation method

The weak form of the heat equation is solved by the finite element (FE) analysis within a time integration scheme [52]

using the commercial software COMSOL to obtain the temperature distribution of the part. As an example, the FE mesh used for discretising the wall geometry is schematically shown in Fig. 7. The elements on the surface are subjected to the convection and radiation boundary conditions given in Eq. (3).

A FE activation scheme is used to model the deposition process, i.e., the growing domain. In this FE activation approach, each element e is assigned a variable x_e to scale the associated thermal conductivity. If x_e is equal to 0 or 1, the finite element is deactivated and activated, respectively. The conductivity κ for an element $e(\kappa_e)$, is given as
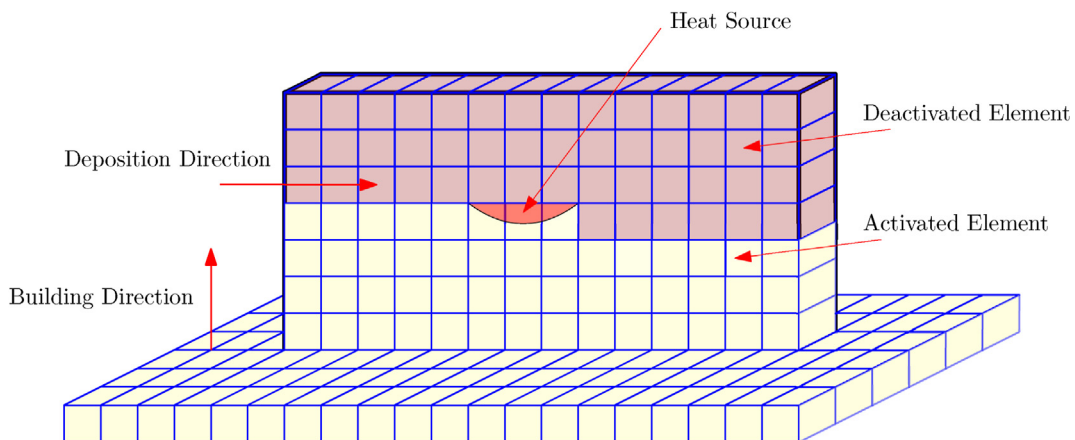

Fig. 7 — Schematic representation of finite element activation method to model material deposition during WAAM. Based on the time and location of the heat source, the deposited elements are activated, represented in yellow. In contrast, the elements of the part that are not yet deposited are kept deactivated, shown in pink.

$$\kappa_e = \kappa_{min} + x_e(\kappa - \kappa_{min}). \tag{6}$$

where, κ_{min} is the minimum conductivity value which is taken as 1×10^{-6} W/mK. The heat source location in Fig. 7 is used to determine which elements are active ($x_e = 1$) at a given time. In contrast, the remaining elements of the layer stay deactivated with $x_e = 0$. For each time step, the location of the heat source changes, and new elements are activated until the deposition is complete. After that, the temperature history at each node of the FE mesh is obtained by a post-processing script.

4. Microstructure prediction

4.1. Solid-state phase transformation

As mentioned in the introduction, the transient thermal history experienced by a material point during the WAAM process consists of multiple heating and cooling cycles. The first cycle corresponds to the deposition of the material in which the metal is melted, deposited, and solidified. After solidification, the most critical solid-state transformation occurs when the parent phase of austenite transforms into the child phases of ferrite, bainite and martensite. For a material point that has already been deposited, subsequent heating and cooling cycles depend on the deposition path, i.e. depending on when material deposition occurs close to the material point of interest. For the thin wall structures we investigate, this phenomenon occurs when the material is deposited near the material point of interest during the deposition of the subsequent layers. If the temperature in the already deposited material point exceeds the Ac_3 temperature in any of the thermal cycles, the child phases transform back to the parent phase austenite. Therefore, the cooling stage after heating for which the temperature of the pre-deposited material exceeds the Ac_3 temperature for the last time becomes critical for determining the fraction and morphology of child phases. In this paper, this is termed the critical cooling stage. The cooling rate of the critical cooling stage is superimposed onto a CCT diagram of the ER110S-G HSLA grade constructed experimentally from the dilatometry measurements to estimate the child phase fractions. The procedure to calculate the phase fractions of the child phases using the CCT diagram is described in the Results and Discussion section.

4.2. Tempering of martensite

Thermal cycles with a peak temperature lower than Ac_3 are unable to transform child phases back to austenite. Although a partial transformation of ferrite to austenite occurs when steel is heated to a temperature between Ac_1 and Ac_3, this effect is neglected for simplicity in this paper. However, heating a material point below Ac_3 can still induce tempering for the martensite phase. If HSLA steel is heated to a temperature above 250 °C, diffusion of carbon from supersaturated martensite leads to the formation of tempered martensite. Tempered martensite has relatively lower hardness and strength but a higher ductility than pristine (untempered) martensite [33]. Hence, determining tempered

martensite fraction is important for a realistic estimation of hardness in WAAM parts. The tempering ratio increases with the tempering temperature and duration which can be accounted for with the JMAK equation as suggested in [53], i.e.

$$X_T = 1 - \exp\left(-(D_0\exp(-Q_t/RT)t)^N\right). \tag{7}$$

Here, t is the tempering duration, T is the tempering temperature, $R = 8.3145$ J/mol/K is the universal gas constant and $Q_t = 1.96 \times 10^5$ J/mol is the activation energy of the tempering process [53]. D_0 and N are the material constants determined from the tempering experiments described in Section 2.4.2 for HSLA ER110S-G steel. The tempering ratio X_T of tempered samples is estimated as

$$X_T = \frac{H_T - H_0}{H_\infty - H_0}, \tag{8}$$

where H_T are the measured hardness value of tempered martensite and H_0 and H_∞ are the hardness values measured at $X_T = 0$ and $X_T = 1$, respectively. The tempering ratio of 0 and 1 indicates pure martensite and fully tempered martensite, respectively. The hardnesses of the fully tempered martensite and untempered martensite are experimentally determined as $H_\infty = 271.3 \pm 3.3$ HV and $H_0 = 389.6 \pm 3.5$ HV respectively.

4.3. Hardness estimation

After the calculation of the phase fractions of all the phases, first using the CCT diagram and then using Eq. (7), it remains to estimate the hardness using the rule of mixture given as follows

$$HV = f_F H_F + f_B H_B + f_M H_M + f_{TM} H_{TM}. \tag{9}$$

Here, f_F, f_B, f_M and f_{TM} are the phase fractions of ferrite, bainite, martensite and tempered martensite, respectively. H_F, H_B, H_M and H_{TM} are the Vicker hardness of the corresponding individual phases. The hardness of the individual phases is evaluated using slightly modified correlations given in [45]. This correlation is used because it is valid for the low-carbon steels but developed for the conventional manufacturing processes which exhibit lower cooling rates than WAAM. Therefore, the correlation is modified to account for high cooling rates. In the modified correlation, an average cooling rate is evaluated in a specific temperature range, in contrast to the cooling rate evaluated at a specific temperature [45]. The modified correlation is as follows

$$
\begin{aligned}
H_M = \ & 127 + 949\text{C} + 27\text{Si} + 11\text{Mn} + 8\text{Ni} \\
& +16\text{Cr} + 21\log(\text{C}/\text{C}_0), \\
H_B = \ & 323 + 185\text{C} + 330\text{Si} + 153\text{Mn} + 65\text{Ni} \\
& +144\text{Cr} + 191\text{Mo} \\
& +\log(\text{C}/\text{C}_0)(89 + 53\text{C} - 55\text{Si} - 22\text{Mn} \\
& - 10\text{Ni} - 20\text{Cr} - 33\text{Mo}) \\
H_F = \ & 42 + 223\text{C} + 53\text{Si} + 30\text{Mn} + 12.6\text{Ni} \\
& +7\text{Cr} + 19\text{Mo} \\
& +\log(\text{C}/\text{C}_0)(10 - 19\text{Si} + 4\text{Ni} \\
& + 8\text{Cr} + 130\text{V}).
\end{aligned} \tag{10}
$$

Here, the symbols of the elements indicate the weight percentage of the elements in the chemical composition of the

steel given in Table 2. C is the average cooling rate in °C/h. C_0 is the constant cooling rate equal to 1 °C/h to normalize the units of the quantity on which log(.) is being applied.

5. Results and Discussions

In this section, first, the predicted thermal history will be validated in Section 5.1 by comparing the thermal model predictions with the thermocouple measurements. Subsequently, in Section 5.2 the experimentally constructed CCT diagram is presented. In Section 5.3, the solid-state phase fraction fields are determined using the simulated temperature history and the CCT diagram. Tempering ratio calculation procedure of martensite through JMAK equation and tempering experiments are given in Section 5.4. The estimated phase fractions and tempering ratios for all three samples are discussed in Section 5.5. The optical micrographs of the three wall samples manufactured by WAAM are shown in Section 5.6. An empirical relation described in Section 5.3 predicts the hardness values associated with a mixture of solid phases and is compared with the experimentally attained hardness values of the printed samples in Section 5.7.

5.1. Thermal history validation

In the remainder, the thermocouples which are attached to the substrate, 5th, 10th and 15th layers are labelled as $L00$, $L05$, $L10$ and $L15$, respectively. For each specimen $S1$, $S2$ and $S3$ given in Table 1, there are 4 thermocouples each of which is uniquely identified as $S\#L\#\#$. For example, the thermocouple attached to layer 15 on the specimen $S3$ is identified as $S3L15$. The locations of thermocouples are shown in Fig. 3. The thermal history predicted by the FEA and measured through four thermocouples for specimen $S1$ are superimposed and are shown in Fig. 8. For specimens $S2$ and $S3$, the superimposed results are shown in Appendix A. For specimens $S2$ and $S3$, the thermocouple data are only shown for three thermocouples each. It is because $S2L15$ and $S3L05$ thermocouples burned during the experiments in $S2$ and $S3$, respectively.

Each peak in the plot indicates the deposition of a new layer. Good agreement is observed between the numerical model predictions and the experiments, especially after the first few layers are deposited (see Fig. 8). The peak temperature predictions are well above the thermocouple data ($S1L05$, $S1L10$ and $S1L15$) for the first few peaks. In the first peak, temperatures are expected to exceed the melting point, around 1500 °C. However, the maximum temperature measured from the K-type thermocouples used in our study is 1200 °C. Moreover, the thermocouple is carefully placed away from fusion zone to avoid damage to the thermocouple. These factors contribute in not capturing the first temperature peaks. Secondly, in K-type thermocouples, the time it takes to reach the 63% of the value of the temperature it is measuring is equal to 0.02 s. Since the heating rates in the first few layers are typically on the order of 10^3 °C/s, the thermocouple measurements are expected to underestimate the peak temperature. We note in passing that the discrepancy diminishes after

a few peaks because the heating and cooling rates and the peak temperatures both decrease. The effects mentioned above are not so dominant for the thermocouple attached to the substrate. Therefore, the superposition of the numerical and experimental data best matches the thermocouple attached to the substrate (see Fig. 8a).

The thermal history is post-processed to identify the critical cooling cycle for each material point. The dotted line indicates the Ac_3 temperature in Fig. 8. Recall that the cooling rate after the last time, the temperature exceeds Ac_3, is considered the critical cooling rate. The region before the critical cooling cycle is termed the reset region, while the region after the critical cooling cycle is the tempering region. The thermal cycles in the latter region transform martensite to tempered martensite, granted the martensite phase is among the child phases during the critical cooling cycle.

Fig. 9a shows the average critical cooling rates between the temperature range 800 °C to 300 °C($C_{8|3}$), estimated by the numerical thermal model along the line in z direction passing through the thermocouples. The cooling rates are high near the substrate and reduced for layers further away from the substrate. This is because the substrate acts as a heat sink and facilitates rapid heat evacuation for the layers deposited close to it. Actual cooling rates close to the substrate are also measured and reported in the literature, showing similar observations [15]. A comparison of the cooling rates obtained from the numerical analysis and experimental measurements is shown in Fig. 9b. The cooling rates are shown after the first 5 layers for better visualisation. For all the samples, the predicted cooling rates are higher than the measured counterparts, as shown in Fig. 9b. The measured cooling rates are 25 – 50% lower than the predicted cooling rates. However, the qualitative trends along the height of the walls are well captured. The lower cooling rate observed in the experimental measurements can be attributed to the before mentioned poor ability of thermocouples to capture the temperature peaks. The discrepancy in the cooling rate measurements and numerically obtained cooling rates becomes less severe once the peak temperature is well captured.

It remains to rationalise the different cooling rates for the various specimens considered in the study. The cooling rates observed in the thin wall are higher than in the thick and tapered walls. This is because the heat input in the thin wall is considerably lower than in the thick and tapered wall promoting a higher cooling rate. Moreover, the predicted cooling rates of the tapered wall for the topmost layers of the specimen are slightly higher than the thick straight wall. As the length of the deposited layer decreases after every deposited layer in the tapered wall, more solid material underneath the deposited layer is available for heat conduction, promoting higher cooling rates at the top layers of the tapered wall compared to the thick wall. This effect is visible both in the experimentally measured and numerically predicted cooling rates. It is also worth noting the effect of tapering is anticipated to be more pronounced near the edges of the specimen than the centre where the thermocouples are situated.

Various parameters are carefully chosen in the numerical thermal model to achieve good agreement with the experimental data. These parameters involve the arc efficiency of
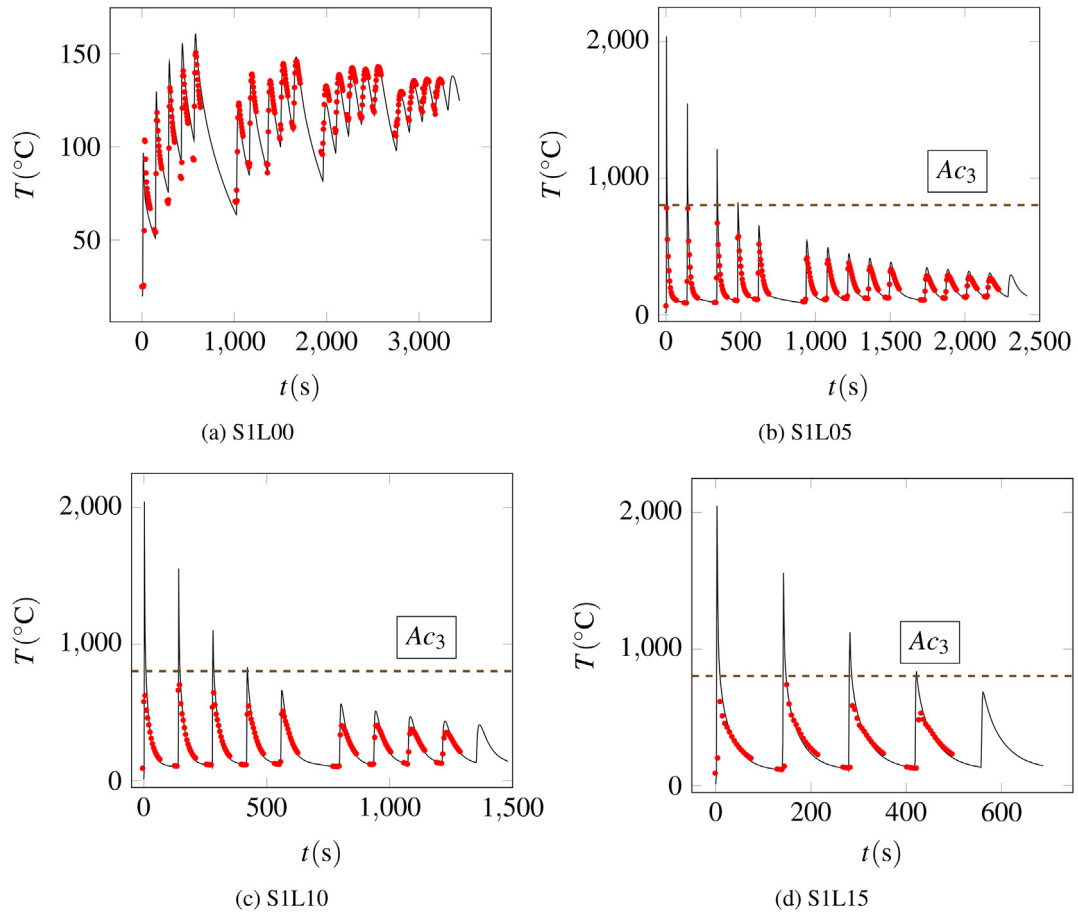
Fig. 8 − Temperature data from thermocouples at (a) substrate, (b) 5th layer, (c) 10th layer and (d) 15th layer associated with specimen S1 (red data points). Temperature predictions calculated with FEA are depicted with a solid black line and thermocouple measurements are illustrated with red points. The black dots denote the thermocouple data points used to calculate the critical cooling rate to compare it with the numerically simulated thermal cooling rates for validation purposes.
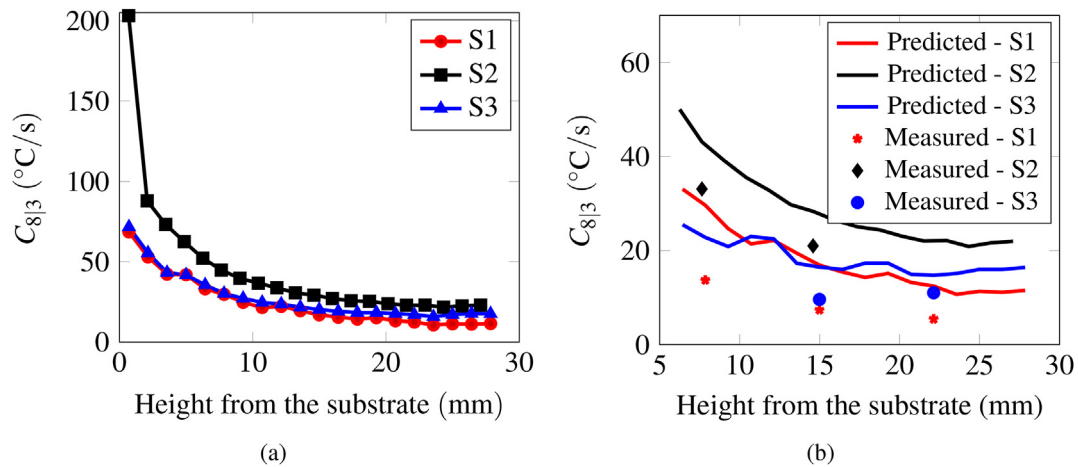

Fig. 9 − (a) Average cooling rate of the critical cycle obtained from the thermal modelling along with the height of the specimen from the substrate. (b) Comparison of the critical cycle cooling rates measured experimentally and obtained from the thermal modelling.

the heat source ($\eta = 0.8$), heat transfer coefficients through the wall and substrate to the surroundings ($h_c = 5.7 \, \text{W/m}^2 - \text{K}$) and thermal material properties as suggested in [47]. All of these parameters impact the thermal history obtained from the simulation. The uncertainties in these parameters will cumulatively impact the numerical predictions of the peak temperature and cooling rates. Through the careful selection of the parameters, the thermal history obtained from numerical FE calculations agrees with thermal data measured from multiple thermocouples. Also, the qualitative trends of cooling rates are well captured. Therefore, the numerical thermal history will be used to predict the solid-state phase fractions in the printed part.

5.2. Dilatometry experiments and CCT diagram

The optical micrographs obtained from the dilatometry samples corresponding to various cooling rates are given in Fig. 10. A qualitative comparison of the optical micrographs indicates the variation in microstructure caused by cooling from the austenitizing temperature at constant cooling rates ranging from 1 °C/s to 330 °C/s. For low cooling rates, coarse grains of ferrite are dominant in the microstructure. The martensite formation in samples cooled at 1 °C/s could be associated with carbon diffusion. The carbon diffuses to the neighbouring austenite grains during ferrite formation, stabilising austenite and subsequent full or partial transformation of remaining
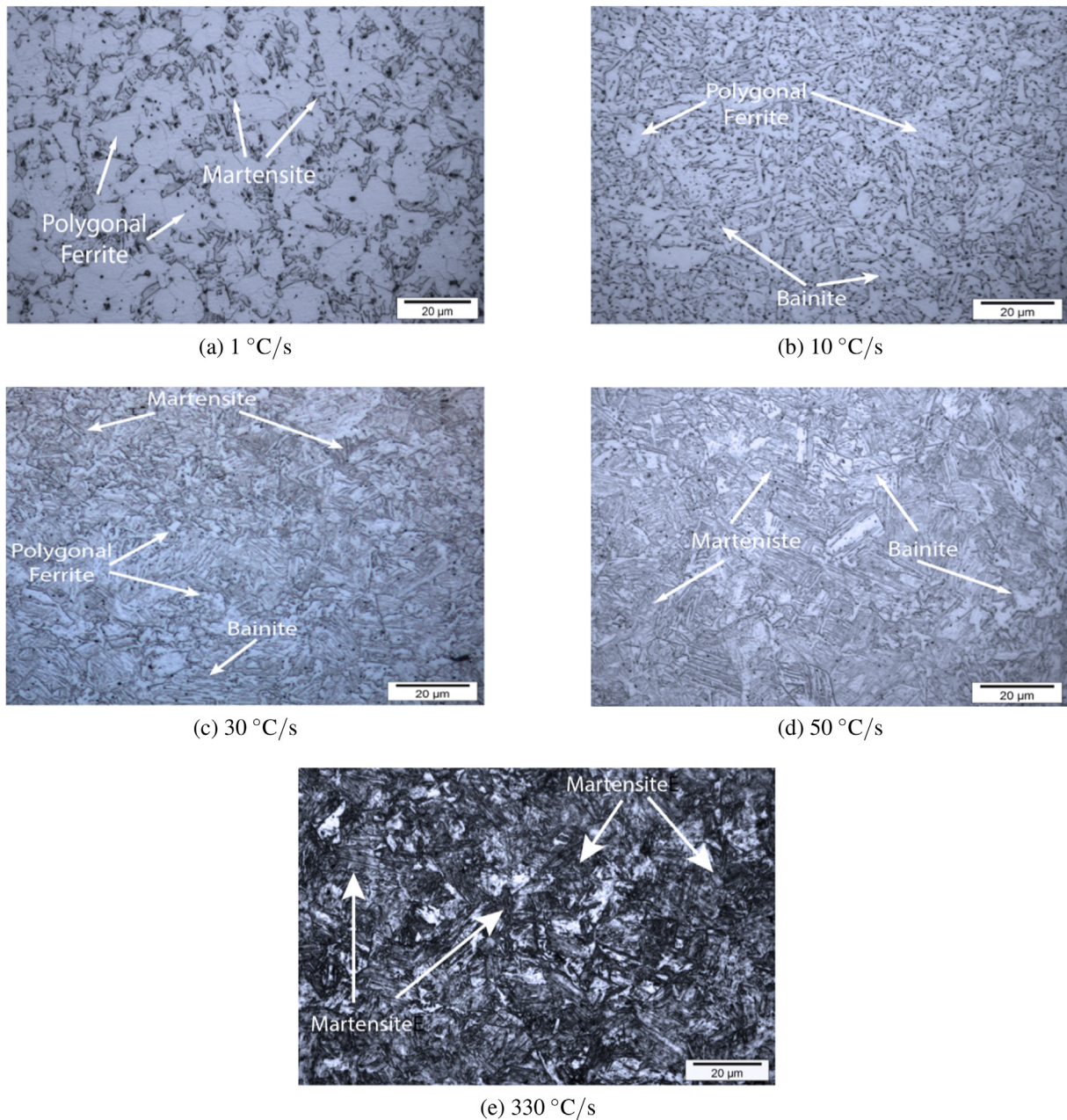

(a) 1 °C/s

(b) 10 °C/s

(c) 30 °C/s

(d) 50 °C/s

(e) 330 °C/s

Fig. 10 – Optical micrographs obtained from dilatometry samples cooled at different cooling rates from austenitization temperature.

austenite to martensite [54]. A mixed microstructure of ferrite and bainite can be seen for the sample subjected to a cooling rate of 10 °C/s. Samples cooled at 30 °C/s have a mixed microstructure of ferrite, bainite, and martensite. As the cooling rate increases to 50 °C/s, the microstructure is a mixture of bainite and martensite with traces of grain boundary ferrite. An increase in martensite fractions can be observed in samples cooled at 10 °C/s to 330 °C/s. A fully martensitic microstructure is observed in the sample cooled at 330 °C/s, indicating the complete transformation of the austenitised sample to martensite.

The raw dilatometry data is shown in Fig. B.1. Each experiment is repeated three times for each cooling rate to ensure repeatability. The resultant fraction of austenite phase (f_A) versus temperature is obtained using the lever rule, discussed in Section 2.4.1, is shown in Fig. B.2. For each cooling rate, a curve fitting operation is performed to evaluate the relation between the phase fraction of austenite and temperature. The curve fitted datasets evaluate the average austenite phase fraction as a function of temperature for the sampled cooling rates, therefore also at a given time, are shown in Fig. 11a. The corresponding measured hardness profiles of the samples are shown in Fig. 11b by a black line.

To construct the Continuous Cooling Transformation (CCT) diagram, the temperature and time values for a given percent of austenite transformed are evaluated from post-processed dilatometry data. Fig. 11a is then converted to a CCT diagram as shown in Fig. 12.

The dotted black lines denote various cooling rates in the experimentally constructed CCT diagram of ER110S-G steel. The red iso-phase lines denote the constant phase fractions across these constant cooling rate profiles. The area engulfed by the iso-phase fraction lines represents where the austenite phase transforms into α phases.

The data obtained from dilatometry are also analysed to identify the temperatures at which the transformation of
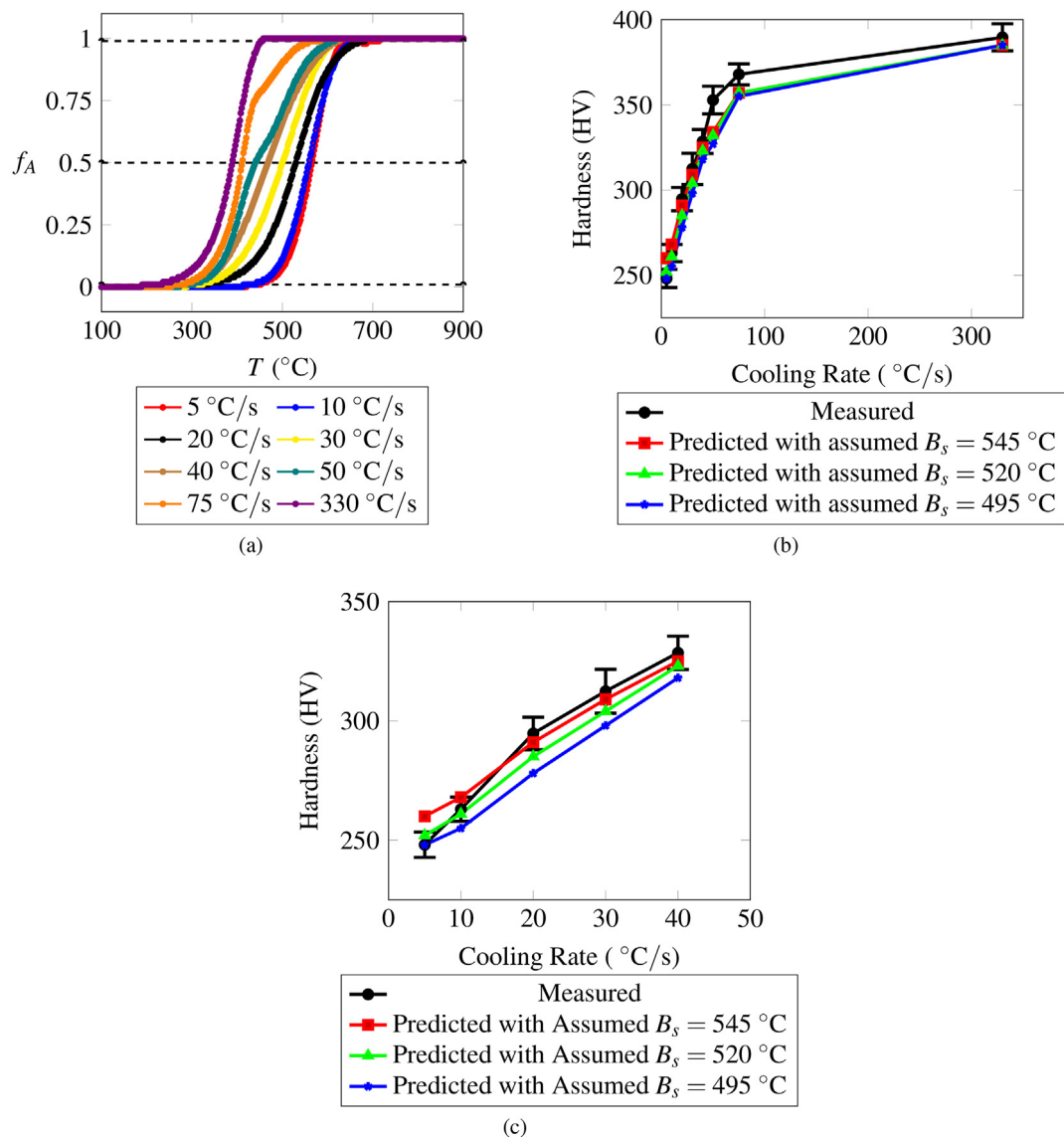

Fig. 11 − (a) Curve fitted dilatometry data obtained for sampled cooling rates. (b) Hardness measurements of the dilatometry samples and a comparison with the predicted hardness evaluated using Eq. (9).
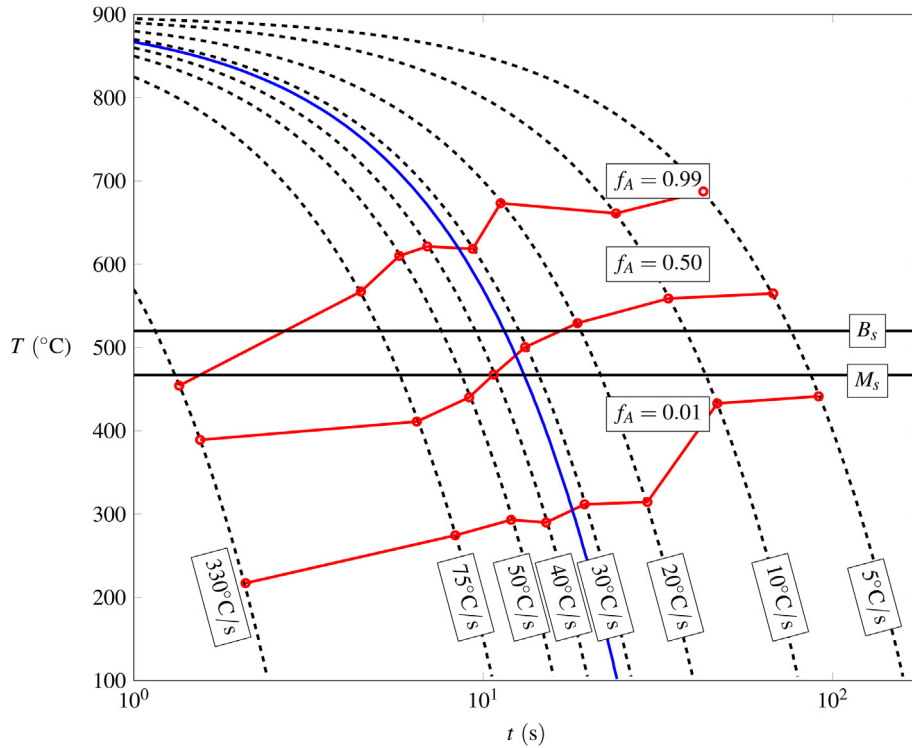
Fig. 12 − **Continuous Cooling Transformation (CCT) diagram obtained from the dilatometry experiments. The dashed black lines represent the cooling rates, and the red lines represent the iso-phase fraction lines of the austenite phase. Solid back lines represent the bainite start temperature (B_s) and martensite start temperature (M_s). Start temperatures are assumed to be independent of the cooling rates.**

phases such as martensite and bainite start. Martensite start temperature (M_s) is evaluated using the dilatometry data corresponding to the highest cooling rate 330 °C/s. At this cooling rate, there is only a single-phase transformation from austenite to martensite, which is also evident from Fig. 10e. Hence, martensite start temperatures can be evaluated by locating the temperature at which the austenite dilatometry curve deviates from linearity. The observed martensite start temperature is 467 °C at 330 °C/s. Also, for cooling rates 75 °C/s and 50 °C/s at approximately the same temperature, a change in slope is observed (see in Fig. 11a). This indicates that the
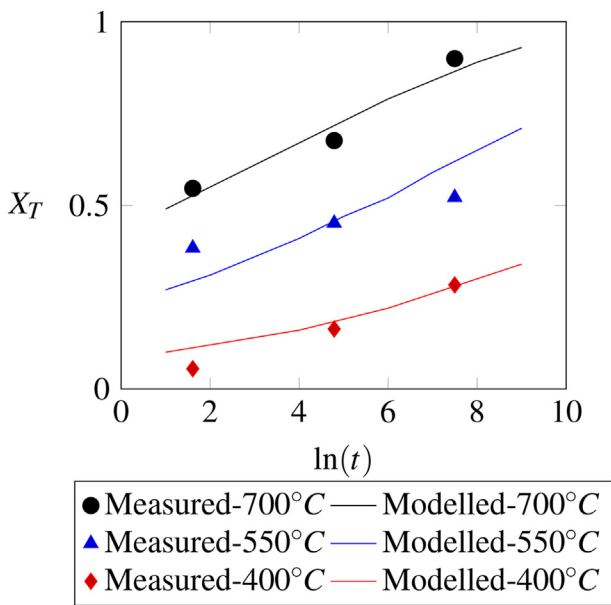

Fig. 13 − **Tempering ratio vs. time obtained from experiments for selected values of tempering temperature and the corresponding predictions obtained from (7).**
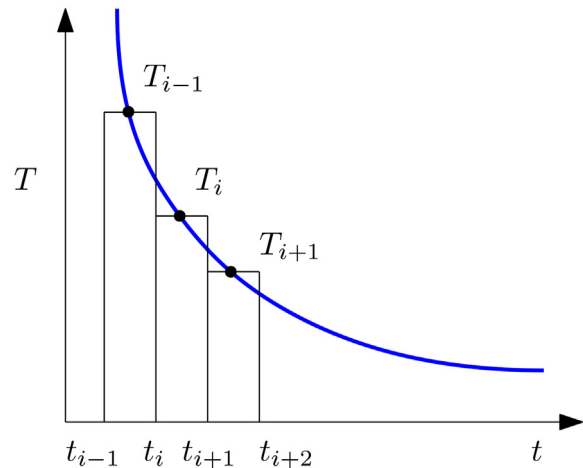

Fig. 14 − **Schematic illustration of a thermal history discretised into isothermal steps.**

martensite starts temperature can be taken as 467 °C and is considered independent of the cooling rate.

To identify the bainite start temperature (B_s), the dilatometry data of intermediate cooling rates such as 20 °C/s, 30 °C/s and 40 °C/s are considered. The dilatometry data of intermediate cooling rates show a plateau type formation in the temperature range where transformation to ferrite and bainite is feasible. The associated micrographs further validate the presence of both ferrite and bainite in Fig. 10. A hit and trial method is used to estimate the bainite start temperature. Firstly, the B_s is assumed to be in a temperature range of 490 °C − 550 °C independent of the cooling rate. Thereafter, for the sampled cooling rates, the corresponding H_M, H_B, and H_F are calculated using the relationship given in Eq. (10). The phase fractions are calculated from the CCT diagram, assuming a trial value of B_s. Finally, the rule of mixtures is applied to predict the hardness value of a dilatometry sample. These predicted hardness values are compared to the experimentally measured hardness of the dilatometry samples. The full

comparison is shown in Fig. 11b. Zooming at low cooling rates are shown in Fig. 11c. The results also imply that the B_s depends on the cooling rate. However, $B_s = 520$ °C gives the best fit for the broad range of samples. Therefore, $B_s = 520$ °C is assumed for simplicity.

5.3.   Solid-state phase fraction estimation

To calculate the phase fraction of the α phases, the average cooling rate for the critical cooling cycle is calculated between 800 °C and 300 °C. Corresponding to the average critical cooling rate, the phase fraction of the austenite is evaluated at the start temperature of the different α phases according to the CCT diagram. For example, the average cooling rate during the critical cooling cycle of the thermal history shown in Fig. 8b is superimposed on the CCT diagram (see Fig. 12) in blue. The blue line first intersects the bainite start temperature B_s, and subsequently the martensite start temperature M_s. The remaining phase fractions of austenite
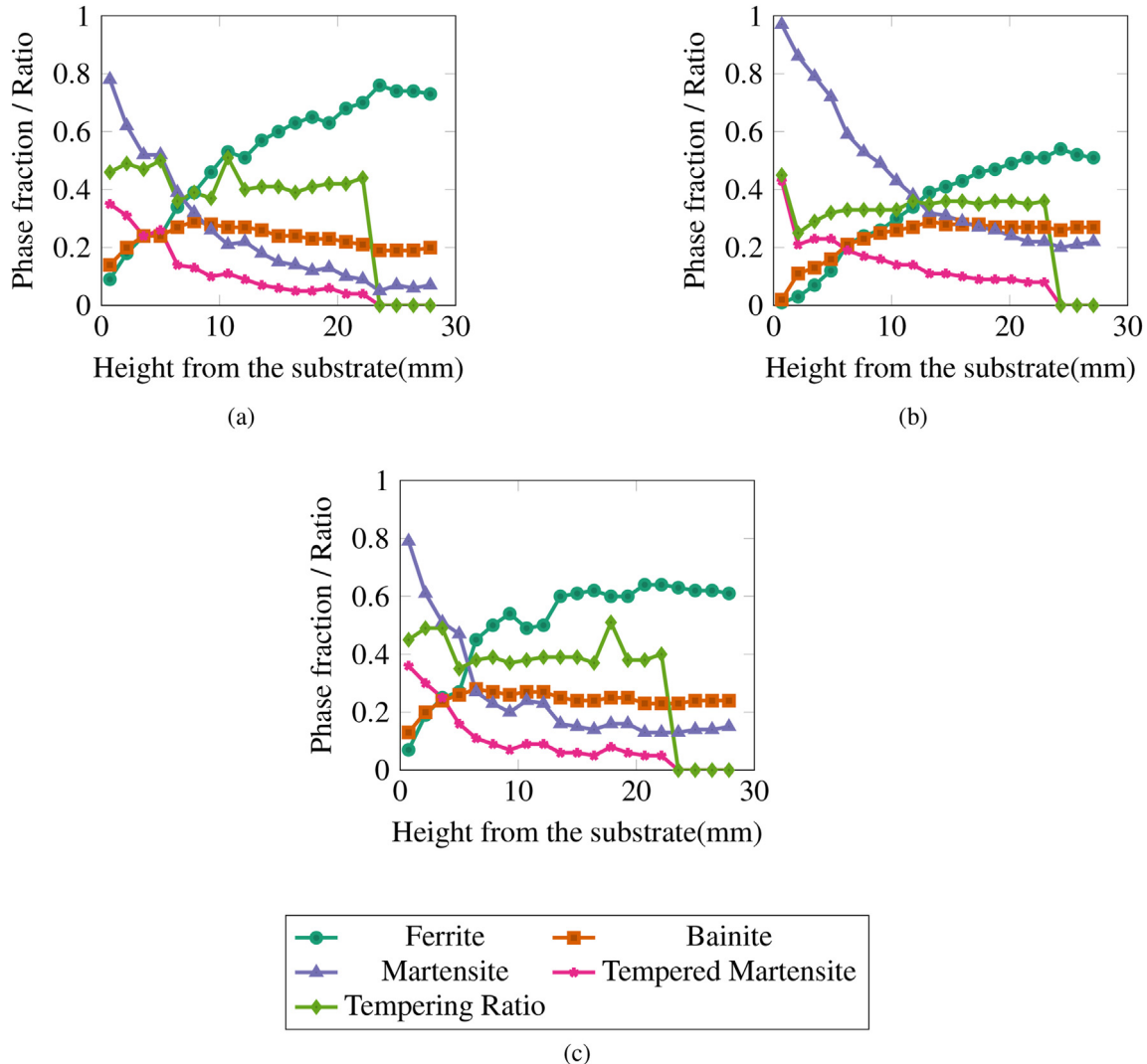

(a)

(b)

(c)

Fig. 15 − **Phase fraction predictions of (a) thick (b) thin, and (c) tapered wall along the centre line of the specimens along to the build direction.**

are calculated at start temperatures B_s and M_s through interpolation. For interpolation the *interp2* function of MATLAB is used. This interpolation function performs linear interpolation between the actual data points and returns the interpolated values at the query point. The query points in our case are the intersection points of the blue line with B_s and M_s. After calculating the phase fractions at query points, the following relation is used to calculate the phase fractions of individual phases

$$
\begin{aligned}
f_f &= 1 - f_A(B_s) \\
f_b &= f_A(B_s) - f_A(M_s) \\
f_m &= f_A(M_s)
\end{aligned}
\tag{11}
$$

5.4.   Martensite tempering

To account for the tempering of the martensite phase, the dilatometry samples containing martensite are subjected to different tempering conditions as mentioned in Section 2.4.2. Experimentally measured hardness values and the corresponding tempering ratios calculated using Eq. (8) are shown in Fig. 13.

At a constant temperature, Eq. (7) can be curve fitted to the experimental data, and the value of D_0 and N can be estimated. For a constant value of $D_0 = 1.179 \times 10^9$ s^{-1} and $N = 0.1695$, Eq. (7) is also plotted in Fig. 13 which shows a good agreement with the experimental data. It remains to use Eq. (7) to predict the degree of tempering in the thermal cycles after the critical cycle. However, the diffusion-based Eq. (7) is only applicable for iso-thermal conditions. Therefore, the thermal cycles where tempering occurs are discretised into isothermal steps as shown in Fig. 14.

Finally, for tempering cycles, the tempering ratio is calculated from the differential form of Eq. (7), which is given as

$$
\dot{X}_T = \frac{(1 - X_T)ND_0\exp(-Q_t/RT)}{(\ln(1/1 - X_T))^{N/(N-1)}}.
\tag{12}
$$

We apply a finite difference scheme in the time domain to solve the above differential equation. The tempering ratio at a particular time is then evaluated as follows.

$$
X_T(t_{i+1}) = \frac{X_T(t_i) + (t_{i+1} - t_i)}{(1 - X_T(t_i))ND_0\exp(-Q_t/RT_i)} \\ \frac{}{(\ln(1/1 - X_T(t_i)))^{N/(N-1)}}.
\tag{13}
$$

A constant time step of $t_{i+1} - t_i = 1 \times 10^{-6}$ s, is used. The time step for tempering calculation is chosen well below the minimum time step used for numerical thermal history evaluation, which is equivalent to 0.03 s. The tempering ratio is then scaled with the martensite's current phase fraction to predict the tempered martensite's phase fraction.

5.5.   Solid state phase fractions and tempering ratio

The phase fraction estimation was performed along the centre line of the specimens along the build direction. This location is selected to minimise the effect of power modulation at the start and stop location during printing. The predicted phase fractions of the α phases are shown in Fig. 15 for all three specimens.

It can be observed in Fig. 15 that the phase fraction of the martensite decreases as the distance from the substrate increases for all specimens. This effect is due to a reduction in the average cooling rate between the critical range of 800 °C − 300 °C ($C_{8|3}$) as the height of the specimen increases. The

(a) Ferrite   (b) Bainite   (c) Martensite

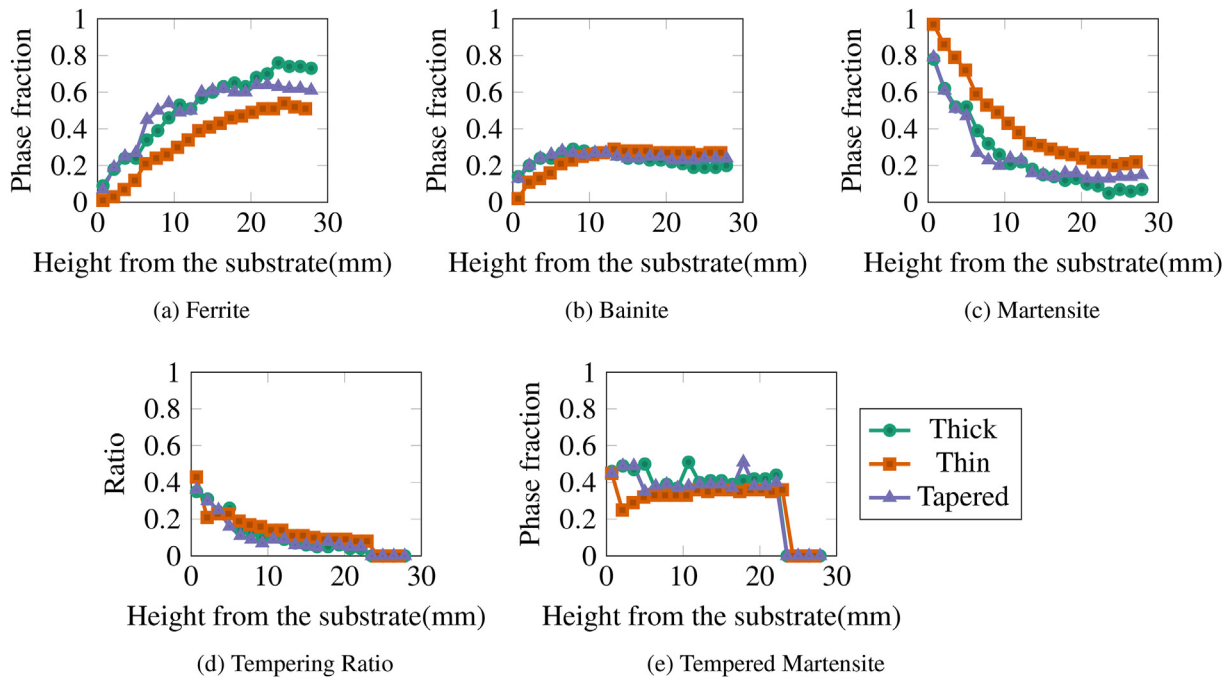(d) Tempering Ratio   (e) Tempered Martensite

Fig. 16 − Comparison of predicted solid state phases fraction of (a) ferrite (b) bainite, and (c) martensite between thick, thin and tapered wall along the line in the z direction passing through the thermocouples shown in Fig. 3. (d) and (e) compares the tempering ratios and phase fraction of tempered martensite of three samples investigated.

average cooling rate for the critical cooling cycle along the part height is shown in Fig. 9.

As the cooling rate decreases, the fraction of phases such as bainite and ferrite increases. The phase fraction of the tempered martensite phase also decreases with the decrease in the martensite phase. The tempering is more pronounced in the layers close to the substrate since these layers experience higher number of heating and cooling cycles than the top layers. No tempering occurs on the topmost layers as there are very few or no tempering cycles after the critical cooling cycle. At the same time, the amount of martensite is small as the cooling rates are diminished.

A comparison of the predicted phase fractions of all three samples is shown in Fig. 16 shows that the ferrite phase fraction is lower for the thin wall than others. The thin wall has more martensite phase fraction compared to other samples due to lower heat input and high cooling rates.

5.6. Optical micrography

The micrographs obtained from the 2nd, 10th and 20th layer are given in Fig. 17. The microstructure of 2nd layer is predominantly composed of martensite, even though ferrite and bainite are present in both thick and tapered samples. However, as the build height increases, the observed martensite phase fractions are lower for all three walls due to the reduction in cooling rates endured by the material. The martensite fractions are the lowest at the top layer for all three walls. A combined microstructure of ferrite, bainite and martensite is observed at the 10th layer for all three walls. This could result from the reduced cooling rate observed in the region 10th layer. Similarly, the microstructure of the 20th layer is also comprised of a mixture of ferrite, bainite and martensite. The 20th layer only undergoes a single thermal cycle but has a lower cooling rate due to the
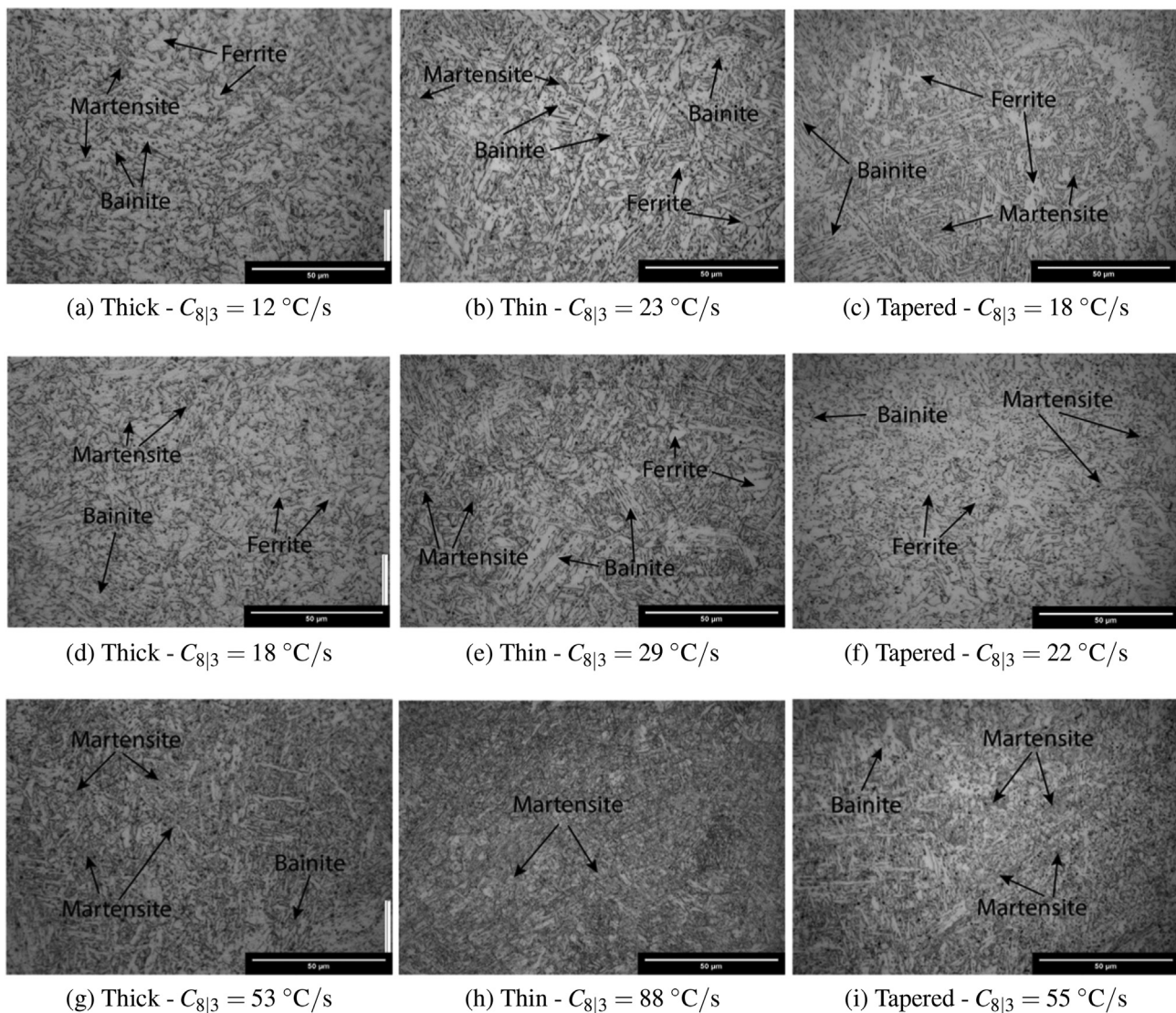

(a) Thick - $C_{8|3} = 12$ °C/s	(b) Thin - $C_{8|3} = 23$ °C/s	(c) Tapered - $C_{8|3} = 18$ °C/s
(d) Thick - $C_{8|3} = 18$ °C/s	(e) Thin - $C_{8|3} = 29$ °C/s	(f) Tapered - $C_{8|3} = 22$ °C/s
(g) Thick - $C_{8|3} = 53$ °C/s	(h) Thin - $C_{8|3} = 88$ °C/s	(i) Tapered - $C_{8|3} = 55$ °C/s

Fig. 17 — Optical micrographs obtained from the AM manufactured thick, thin and tapered walls. The top, middle and the bottom row represents the 20th, 10th and 2nd layer of the printed sample, respectively. The corresponding calculated critical cooling rates are also given.
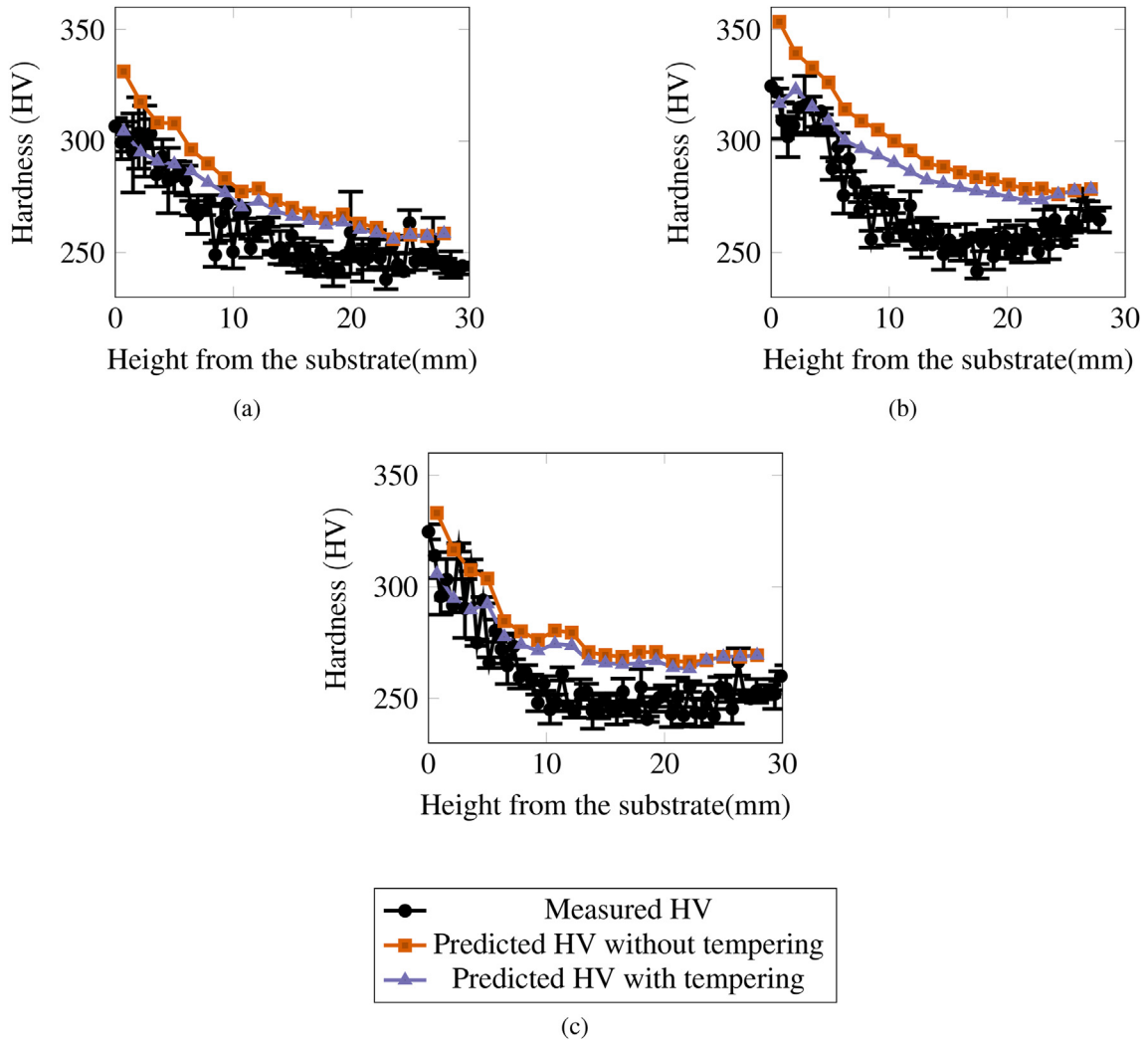
Fig. 18 — **Hardness comparison of the (a) thick (b) thin, and (c) tapered walls.**

lower thermal diffusivity caused by heat accumulation. Therefore, a relatively lower fraction of non-equilibrium phases like bainite and martensite can be observed at 20th layer than at 10th layer.

It can be observed that in Fig. 17h the cooling rate is 88 °C/s. This is higher than the critical cooling rate for fully martensitic transformation. Hence the micrograph from Fig. 17h is comparable to the micrograph from dilatometry experiments
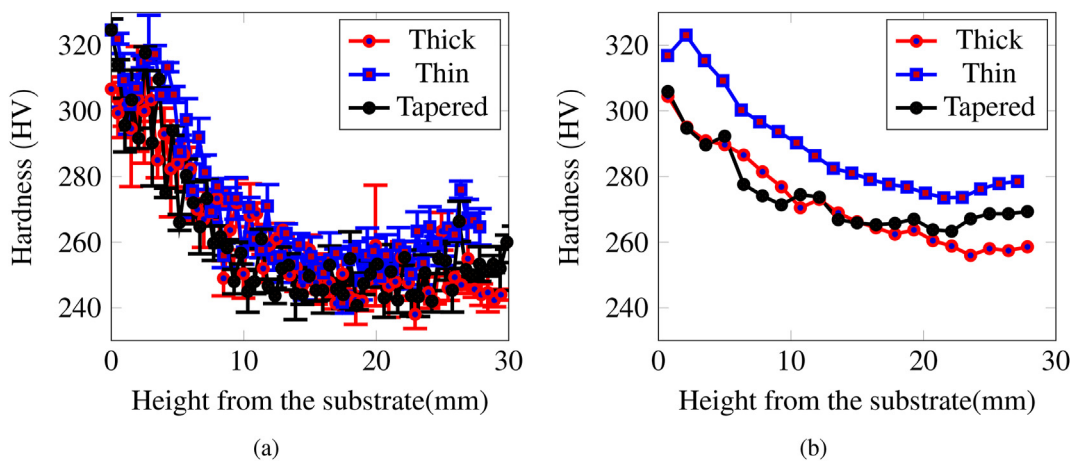

Fig. 19 — **Comparison of (a) experimental and (b) predicted hardness values of thick, thin and tapered samples.**

in Fig. 10 corresponding to a cooling rate of 330 °C/s. The micrographs from the 2nd layer of thick and thin samples look similar to the micrographs from dilatometry corresponding to the cooling rate of 50 °C/s. Additionally, the material points from the 10th and 20th layers of the thick, thin and tapered have undergone cooling rates between 10 °C/s and 20 °C/s. The micrographs from these material points show good comparability with micrographs from dilatometry experiments corresponding to cooling rates of 10 °C/s and 30 °C/s. Note that though Fig. 17c and d have similar cooling rates, the microstructures appear different. The 10th layer undergoes several thermal cycles, remelting, reaustenitization and tempering. However, the material point at 20th layer undergoes only one thermal cycle, resembling the deposition of a single bead and hence gives the microstructure devoid of tempering. The similarity of micrographs with the dilatometry images indicates good correlation between dilatometry samples and the WAAM printed samples. This points to the reliability of the CCT diagram obtained using dilatometry to the WAAM process. Additionally, the optical micrographs indicate good qualitative agreement with predicted phase fractions.

5.7. Hardness comparison

First, the corresponding hardness for the predicted phase fractions will be evaluated using Eq. (9). Subsequently, these hardness predictions are compared with the experimentally measured hardness values as shown in Fig. 18.

Hardness measurements are performed at three points at the same build height to quantify the uncertainties on the measured hardness values. Each of these hardness indents was 1.5 mm apart in the x-direction. The standard deviation of three measurements is calculated and indicated as the error bars in Fig. 18. The measured hardness value decreases as the height of the specimen increases. This suggests a considerable martensite presence in the layers close to the substrate diminishing towards the top. Predicted hardness values also show a similar trend. Moreover, predicted hardness profiles accounting for the tempering show that the effect of tempering is more significant and the degree of tempering is more pronounced in the layers close to the substrate than at the topmost layers as anticipated.

The hardness predictions are in good agreement with the measurements for the layers close to the substrate. Recall that the value of hardness is less sensitive to the high cooling rates as shown in Fig. 11b. The predicted cooling rates for the critical cooling cycles for layers close to the substrate are > 75 °C/s as can be seen in Fig. 9. This will result in a complete phase transformation from austenite to martensite. Therefore, the predicted hardness is reasonably accurate for layers close to the substrate. Cooling rates become moderate or low for the layers away from the substrate, as shown in Fig. 9. The cooling rates of the critical cooling cycle as predicted by the thermal model, are higher than those observed from thermocouples. Though lack of data points at peaks limits this comparison. Lower cooling rates would promote more ferrite content and a reduction in hardness. A possible source of error is the constant Ac_3 temperature assumption in our model. In reality, the Ac_3 temperature depends on the heating rates [55]. Depending on the heating rate, the Ac_3 temperature can change. Based on the

Ac_3 temperature and peak temperature, the critical cooling cycle might shift, impacting the cooling rates and, consequently, the hardness. The critical cooling cycle for the heating rate dependent cases will be the last cooling cycle with peak temperature exceeding Ac_3 corresponding to the heating rate. Furthermore, the uncertainties in the experimental measurements, such as the dilatometry measurements used in the construction of the CCT diagram, start temperature of various α phases, errors associated with the empirical model for hardness predictions and uncertainties in capturing tempering kinetics also contribute to the mismatch between the predicted and measured hardness values.

The comparison of the hardness of all three samples is shown in Fig. 19. The experimental results show that the hardness of the thin specimen is slightly higher than the thick and tapered samples. This can be attributed to the high cooling rates observed in the thin sample due to lower heat input. Comparing the thick and tapered wall shows that the hardness is comparable in the layers close to the substrate. However, top layers of the tapered sample, exhibit a slightly higher hardness than top layers of the thick sample due to a slightly higher cooling rate due to tapering. The comparison of all the samples shows no significant variation in the hardness values due to changes in the process parameters and design.

6. Conclusions

In this study, the correlation between the experimentally validated transient thermal history experienced by the WAAM manufactured HSLA ER110S-G steel part is used to predict the composition of resultant solid-state phases and the corresponding hardness response. Following are some salient points of this study.

- The superimposition of the thermal history measured from the thermocouples to the thermal history obtained from the FE modelling shows good agreement for all three wall specimens. The actual cooling rates calculated from the thermocouple data are 25 − 50% lower than the predicted cooling rates.
- Multiple thermal heating and cooling cycles are experienced by WAAM manufactured parts. The thermal cycles for a material point can be divided into three zones. First is the reset zone, in which the peak temperature of cycles are well above the Ac_3 temperature. Consequently, the microstructure resets to the parent austenite phase in this region. The second zone consists of the critical cycle. The critical cycle is the cooling part of the last thermal cycle with a peak temperature higher than the Ac_3 temperature. The solid phase transformation from the parent austenite phase to child phases such as ferrite, bainite and martensite happens due to this critical cycle. The third zone is the tempering zone in which the martensite transforms into tempered martensite.
- The predicted fractions of the solid-state phases in the microstructure depend on the cooling rate of the critical cooling cycle. High cooling rates result in microstructure with a high fraction of martensite phase and low cooling rates result in bainite and ferrite-dominated

microstructures. This is validated through the superimposition of the predicted microhardness and measured microhardness of the AM samples. The results show that predicted hardness are in the acceptable limit for regions with high cooling rates. The predicted hardness is 10% higher than the measured hardness which is attributed to the over-prediction of the cooling rates.

- The effect of tempering is significant in the regions where the martensite content is dominant and the regions experience more tempering cycles. The tempering contributed to reduce the microhardness by 8 − 10% in the regions with high martensite percentage.
- Comparison of the AM samples with approximately similar critical cooling rates in the temperature range of 800 °C-300 °C show similar microstructural features. The microstructural features of AM samples are also similar to dilatometry samples which are subjected to constant cooling rates from the austenitization temperature.
- Comparing the hardness of all specimens shows that at the investigated location the effect of the process parameters and design are not significant. This can be attributed to the lack of a significant effect on the cooling rates of the critical cycle.
- In addition, the developed model is very general and applicable across different materials given, the thermal

properties of the material and the CCT diagram are available.

Declaration of competing interest

The authors declare that they have no known competing financial interests or personal relationships that could have appeared to influence the work reported in this paper.

Acknowledgements

Appendix A. Thermal history comparison

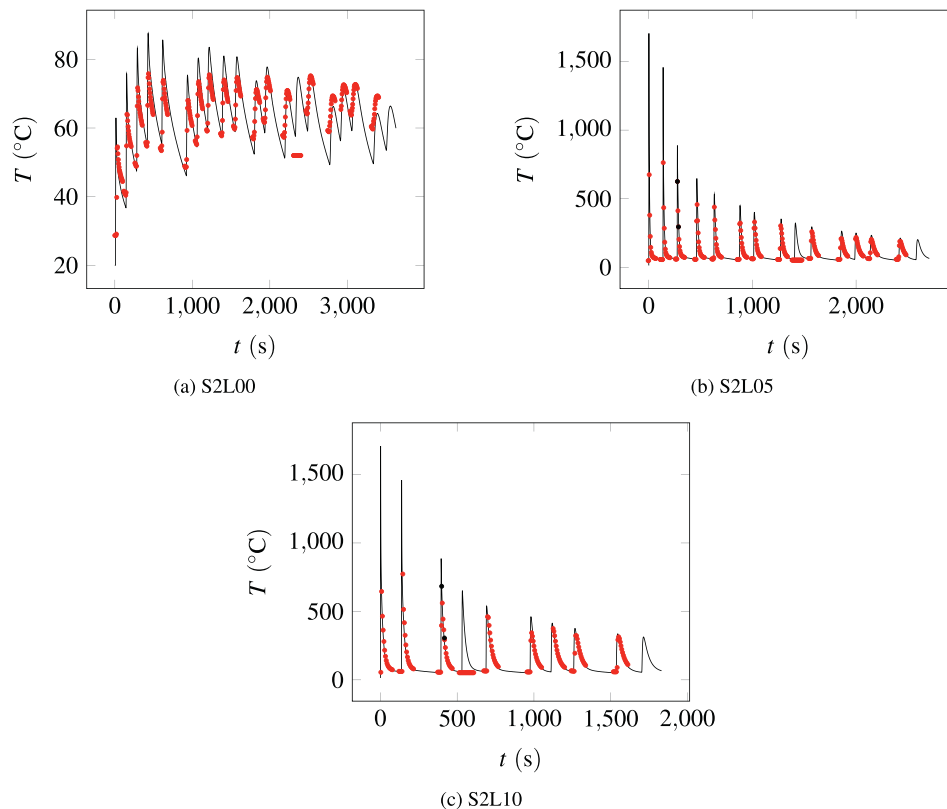(a) S2L00

(b) S2L05

(c) S2L10

Figure A.1 − Temperature Data from thermocouples associated to specimen S2 (red data points) compared with the thermal history obtained from the thermal modelling (black solid line). The black dots denote the thermocouple data points which are used to calculate the cooling rate of the critical cycle from the experimental data.

(a) S3L00

(b) S3L10

(c) S3L15

Figure A.2 − **Temperature Data from thermocouples associated to specimen S3 (red data points) compared with the thermal history obtained from the thermal modelling (black solid line). The black dots denote the thermocouple data points which are used to calculate the cooling rate of the critical cycle from the experimental data.**
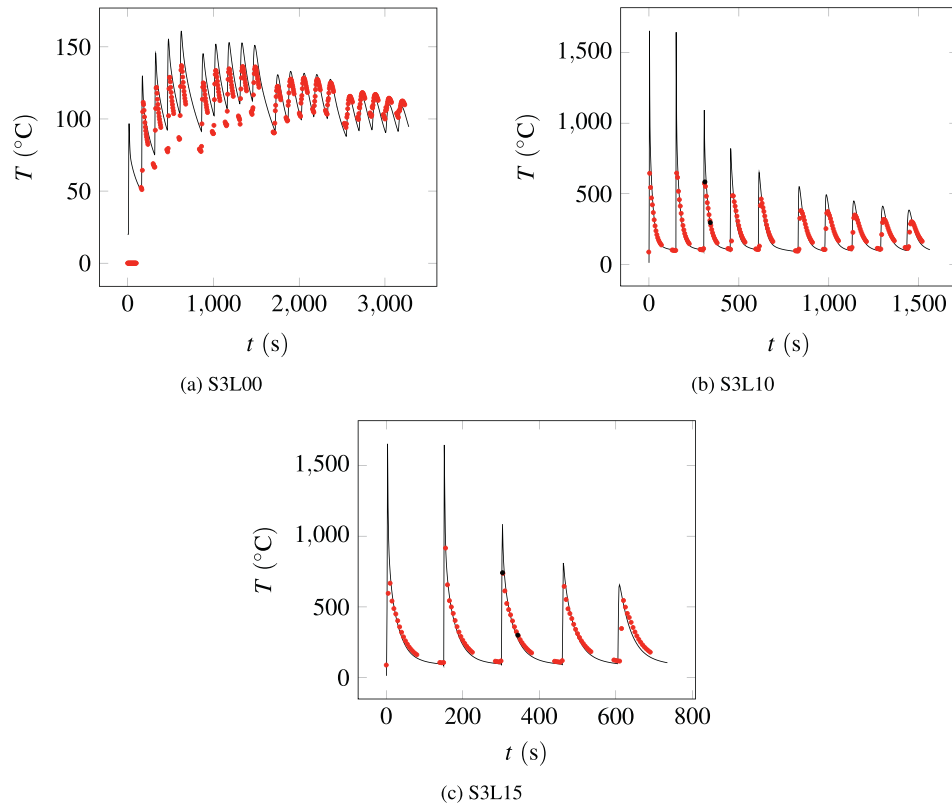
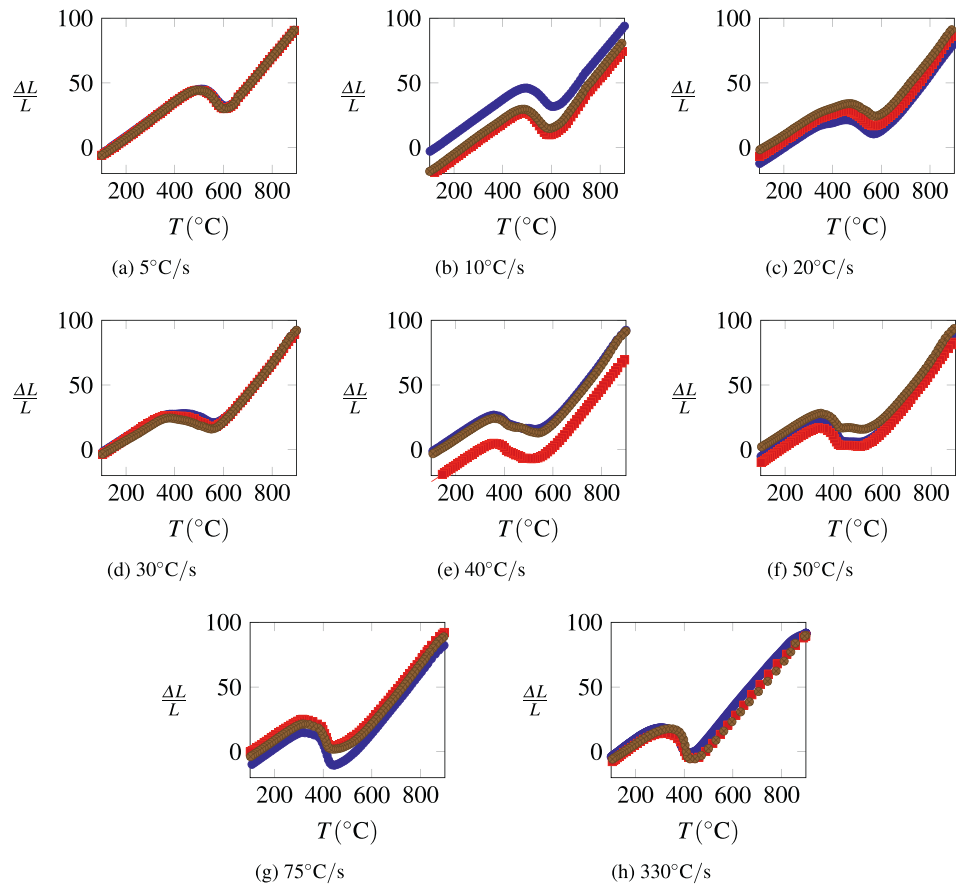**Appendix B. Raw Data Dilatometry**

Figure B.1 — **Raw Dilatometry Data for different cooling rate. For each cooling rate 3 sets of data are generated.**
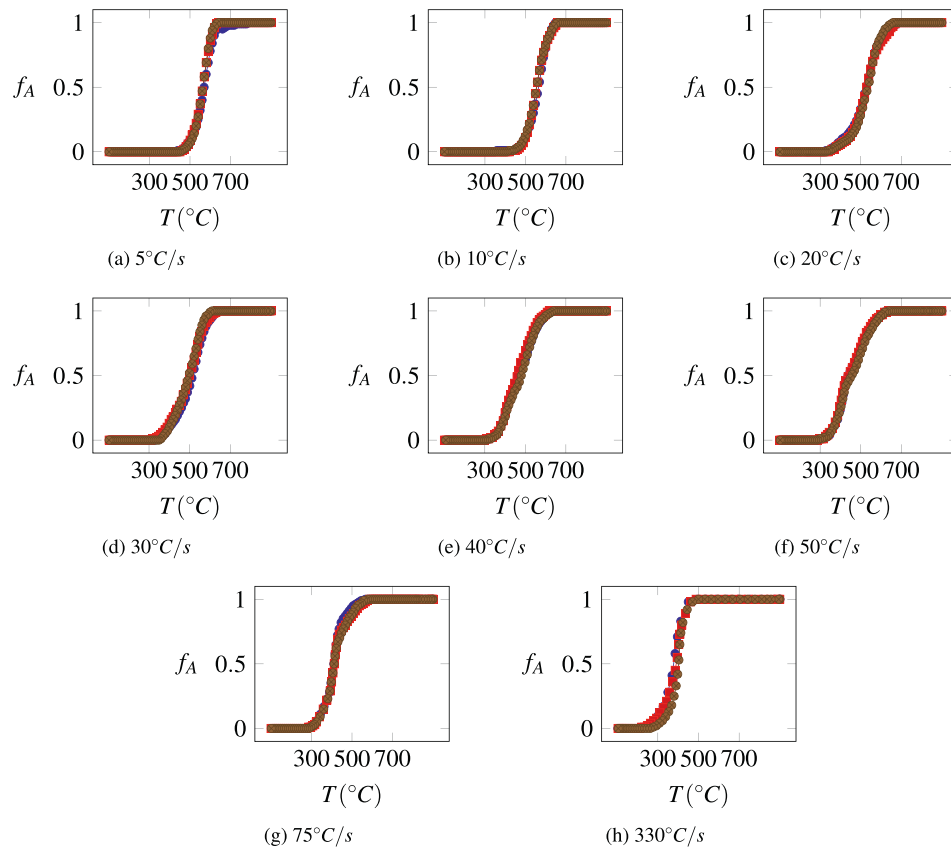
(a) 5°C/s

(b) 10°C/s

(c) 20°C/s

(d) 30°C/s

(e) 40°C/s

(f) 50°C/s

(g) 75°C/s

(h) 330°C/s

Figure B.2 − Austenite phase fraction (v_A) as the function of Temperature calculated from the dilatometry data using the lever rule.

REFERENCES

[1] Knezović N, Topić A. Wire and Arc Additive manufacturing (WAAM)−a new advance in manufacturing. In: International conference "new technologies, development and applications". Springer; 2018. p. 65−71.

[2] Ding J, Martina F, Williams S. Production of large metallic components by additive manufacture−issues and achievements. In: Conf. Pap.; nov; 2015.

[3] Wu B, Pan Z, Ding D, Cuiuri D, Li H, Xu J, et al. A review of the wire arc additive manufacturing of metals: properties, defects and quality improvement. J Manuf Process 2018;35:127−39.

[4] Bendsoe MP, Sigmund O. Topology optimization: theory, methods, and applications. Springer Science & Business Media; 2013.

[5] Song GH, Lee CM, Kim DH. Investigation of path planning to reduce height errors of intersection parts in wire-Arc Additive manufacturing. Materials 2021;14(21):6477.

[6] Venturini G, Montevecchi F, Bandini F, Scippa A, Campatelli G. Feature based three axes computer aided manufacturing software for wire arc additive manufacturing dedicated to thin walled components. Addit Manuf 2018;22:643−57.

[7] Venturini G, Montevecchi F, Scippa A, Campatelli G. Optimization of WAAM deposition patterns for T-crossing features. Procedia Cirp 2016;55:95−100.

[8] Ding D, Pan Z, Cuiuri D, Li H. A practical path planning methodology for wire and arc additive manufacturing of thin-walled structures. Robot Comput Integrated Manuf 2015;34:8−19.

[9] Rauch M, Hascoet JY, Querard V. A multiaxis tool path generation approach for thin wall structures made with WAAM. Journal of Manufacturing and Materials Processing 2021;5(4):128.

[10] Liu J, Gaynor AT, Chen S, Kang Z, Suresh K, Takezawa A, et al. Current and future trends in topology optimization for additive manufacturing. Struct Multidiscip Optim 2018;57(6):2457−83.

[11] Wu B, Pan Z, Ding D, Cuiuri D, Li H. Effects of heat accumulation on microstructure and mechanical properties of Ti6Al4V alloy deposited by wire arc additive manufacturing. Addit Manuf 2018;23:151−60.

[12] Wang L, Xue J, Wang Q. Correlation between arc mode, microstructure, and mechanical properties during wire arc additive manufacturing of 316L stainless steel. Mater Sci Eng, A 2019;751:183−90.

[13] Su C, Chen X, Gao C, Wang Y. Effect of heat input on microstructure and mechanical properties of Al-Mg alloys fabricated by WAAM. Appl Surf Sci 2019;486:431−40.

[14] Aldalur E, Veiga F, Suárez A, Bilbao J, Lamikiz A. High deposition wire arc additive manufacturing of mild steel: strategies and heat input effect on microstructure and mechanical properties. J Manuf Process 2020;58:615−26.

[15] Rodrigues TA, Duarte V, Avila JA, Santos TG, Miranda R, Oliveira J. Wire and arc additive manufacturing of HSLA steel: effect of thermal cycles on microstructure and mechanical properties. Addit Manuf 2019;27:440−50.

[16] Hejripour F, Binesh F, Hebel M, Aidun DK. Thermal modeling and characterization of wire arc additive manufactured duplex stainless steel. J Mater Process Technol 2019;272:58−71.

[17] Gornyakov V, Sun Y, Ding J, Williams S. Efficient determination and evaluation of steady-state thermal–mechanical variables generated by wire arc additive manufacturing and high pressure rolling. Model Simulat Mater Sci Eng 2021;30(1):014001.

[18] Ding J, Colegrove P, Mehnen J, Williams S, Wang F, Almeida PS. A computationally efficient finite element model of wire and arc additive manufacture. Int J Adv Manuf Technol 2014;70(1–4):227–36.

[19] Yildiz AS, Davut K, Koc B, Yilmaz O. Wire arc additive manufacturing of high-strength low alloy steels: study of process parameters and their influence on the bead geometry and mechanical characteristics. Int J Adv Manuf Technol 2020;108(11):3391–404.

[20] Rodideal N, Machado CM, Infante V, Braga DF, Santos TG, Vidal C. Mechanical characterization and fatigue assessment of wire and arc additively manufactured HSLA steel parts. Int J Fatig 2022;164:107146.

[21] Duarte VR, Rodrigues TA, Schell N, Santos TG, Oliveira JP, Miranda RM. Wire and arc additive manufacturing of high-strength low-alloy steel: microstructure and mechanical properties. Adv Eng Mater 2021;23(11):2001036.

[22] Mehnen J, Ding J, Lockett H, Kazanas P. Design study for wire and arc additive manufacture. Int J Product Develop 20 2014;19(1–3):2–20.

[23] McAndrew AR, Rosales MA, Colegrove PA, Hönnige JR, Ho A, Fayolle R, et al. Interpass rolling of Ti-6Al-4V wire+ arc additively manufactured features for microstructural refinement. Addit Manuf 2018;21:340–9.

[24] Mishra V, Ayas C, Langelaar M, van Keulen F. Controlling cooling rates through topology optimization for required microstructure in additive manufacturing process. In: 2022 ASPE and euspen summer topical meeting on advancing precision in additive manufacturing. ASPE; 2022. p. 8–12.

[25] Ayed A, Valencia A, Bras G, Bernard H, Michaud P, Balcaen Y, et al. Effects of WAAM process parameters on metallurgical and mechanical properties of Ti-6Al-4V deposits. In: Advances in materials, mechanics and manufacturing. Springer; 2020. p. 26–35.

[26] Foster B, Beese A, Keist J, McHale E, Palmer T. Impact of interlayer dwell time on microstructure and mechanical properties of nickel and titanium alloys. Metall Mater Trans 2017;48(9):4411–22.

[27] Silva RHG, Rocha PCJ, Rodrigues MB, Pereira M, Galeazzi D. Analysis of interlayer idle time as a temperature control technique in additive manufacturing of thick walls by means of CMT and CMT pulse welding processes. Soldagem & Inspeção 2020:25.

[28] Müller J, Hensel J, Dilger K. Mechanical properties of wire and arc additively manufactured high-strength steel structures. Weld World 2022;66(3):395–407.

[29] Dirisu P, Ganguly S, Mehmanparast A, Martina F, Williams S. Analysis of fracture toughness properties of wire+ arc additive manufactured high strength low alloy structural steel components. Mater Sci Eng, A 2019;765:138285.

[30] Xin H, Correia JA, Veljkovic M, Zhang Y, Berto F, de Jesus AM. Probabilistic strain-fatigue life performance based on stochastic analysis of structural and waam-stainless steels. Engineering Failure Analysis; 2021, 105495.

[31] DebRoy T, Wei H, Zuback J, Mukherjee T, Elmer J, Milewski J, et al. Additive manufacturing of metallic components—process, structure and properties. Prog Mater Sci 2018;92:112–224.

[32] Callister Jr WD, Rethwisch DG. Callister's materials science and engineering. John Wiley & Sons; 2020.

[33] Bhadeshia H, Honeycombe R. Steels: microstructure and properties. Butterworth-Heinemann; 2017.

[34] Huang C, Kyvelou P, Zhang R, Britton TB, Gardner L. Mechanical testing and microstructural analysis of wire arc additively manufactured steels. Mater Des 2022;216:110544.

[35] Sun L, Jiang F, Huang R, Yuan D, Guo C, Wang J. Anisotropic mechanical properties and deformation behavior of low-carbon high-strength steel component fabricated by wire and arc additive manufacturing. Mater Sci Eng, A 2020;787:139514.

[36] Haden C, Zeng G, Carter III F, Ruhl C, Krick B, Harlow D. Wire and arc additive manufactured steel: tensile and wear properties. Addit Manuf 2017;16:115–23.

[37] Elahi S, Tavakoli R, Romero I, Tourret D. Grain growth competition during melt pool solidification—comparing phase-field and cellular automaton models. Comput Mater Sci 2023;216:111882.

[38] Lian Y, Lin S, Yan W, Liu WK, Wagner GJ. A parallelized three-dimensional cellular automaton model for grain growth during additive manufacturing. Comput Mech 2018;61(5):543–58.

[39] Teferra K, Rowenhorst DJ. Optimizing the cellular automata finite element model for additive manufacturing to simulate large microstructures. Acta Mater 2021;213:116930.

[40] Yang M, Wang L, Yan W. Phase-field modeling of grain evolutions in additive manufacturing from nucleation, growth, to coarsening. Npj Computational Materials 2021;7(1):1–12.

[41] Rodgers TM, Madison JD, Tikare V. Simulation of metal additive manufacturing microstructures using kinetic Monte Carlo. Comput Mater Sci 2017;135:78–89.

[42] van Nuland TF, van Dommelen J, Geers MG. Microstructural modeling of anisotropic plasticity in large scale additively manufactured 316L stainless steel. Mech Mater 2021;153:103664.

[43] Zhang Q, Xie J, Gao Z, London T, Griffiths D, Oancea V. A metallurgical phase transformation framework applied to SLM additive manufacturing processes. Mater Des 2019;166:107618.

[44] Goldak J, Chakravarti A, Bibby M. A new finite element model for welding heat sources. Metall Trans A B 1984;15(2):299–305.

[45] Doane DV. Application of hardenability concepts in heat treatment of steel. J Heat Treat 1979;1(1):5–30.

[46] Wu Kuo-Hao. 3D additive manufacturing: microstructural evolution of HSLA steel in WAAM process. 2020. Available from, http://repository.tudelft.nl/.

[47] Gao H. Residual stress development due to high-frequency post weld impact treatments for high-strength steels. Delft University of Technology; 2018.

[48] DuPont JN, Marder AR. Thermal efficiency of arc welding processes. Welding J Including Welding Res Supplement 1995;74(12):406s.

[49] Moyer J, Ansell G. The volume expansion accompanying the martensite transformation in iron-carbon alloys. Metall Trans A 1975;6(9):1785–91.

[50] Suh DW, Oh CS, Han HN, Kim SJ. Dilatometric analysis of austenite decomposition considering the effect of non-isotropic volume change. Acta Mater 2007;55(8):2659–69.

[51] Yang Y, Zhou X, Li Q, Ayas C. A computationally efficient thermo-mechanical model for wire Arc Additive manufacturing. Additive Manufacturing; 2021, 102090.

[52] Hughes TJ, Liu W. Implicit-explicit finite elements in transient analysis: stability theory. 1978.

[53] Sun Y, Obasi G, Hamelin C, Vasileiou A, Flint T, Francis J, et al. Characterisation and modelling of tempering during multi-pass welding. J Mater Process Technol 2019;270:118–31.

[54] Thompson SW. Continuous cooling transformation behavior in HSLA80 steel. Metall Mater Trans 1996;27(6):1557–71.

[55] FG C Capdevila C, De Andres CG. An attempt to establish the variables that most directly influence the austenite formation process in steels. ISIJ Int 2003;43(5):726–35.